

Geochemistry, Geophysics, Geosystems

RESEARCH ARTICLE

10.1029/2018GC007905

Key Points:

- A new approach is designed to document shear wave travel times, waveform shape and quality, and other measurements
- A global high-quality shear wave data set of over 250 K waveforms was constructed, and all measurements are made available
- Quantitative measurements of variable waveform widths more accurately document seismic wave onset times

Supporting Information:

- Supporting Information S1
- Table S1

Correspondence to:

H. Lai,
hongyu.lai@asu.edu

Citation:

Lai, H., Garnero, E. J., Grand, S. P., Porritt, R. W., & Becker, T. W. (2019). Global travel time data set from adaptive empirical wavelet construction. *Geochemistry, Geophysics, Geosystems*, 20. <https://doi.org/10.1029/2018GC007905>

Received 14 AUG 2018

Accepted 31 MAR 2019

Accepted article online 02 APR 2019

Global Travel Time Data Set From Adaptive Empirical Wavelet Construction

Hongyu Lai¹ , Edward J. Garnero¹, Stephen P. Grand², Robert W. Porritt³ , and Thorsten W. Becker^{2,3} 

¹School of Earth and Space Exploration, Arizona State University, Tempe, AZ, USA, ²Department of Geological Sciences, Jackson School of Geosciences, University of Texas at Austin, Austin, TX, USA, ³Institute for Geophysics, Jackson School of Geosciences, The University of Texas at Austin, Austin, TX, USA

Abstract We present a method for constructing the average waveform shape (hereafter called “empirical wavelet”) of seismic shear waves on an event-by-event basis for the purpose of constructing a high-quality travel time data set with information about waveform quality and shape. A global data set was assembled from 360 earthquakes between 1994 and 2017. The empirical wavelet approach permits documentation of the degree of similarity of every observed wave with the empirical wavelet. We adapt the empirical wavelet to all pulse widths, thus identifying broadened (e.g., attenuated) pulses. Several measures of goodness of fit of the empirical wavelet to each record are documented, as well as signal-to-noise ratios, permitting users of the data set to employ flexible weighting schemes. We demonstrate the approach on transversely polarized SH waves and build a global travel time data set for the waves S, SS, SSS, Sdiff, ScS, and ScSScS. Onset arrival times of the waves were determined through a correlation scheme with best-fitting empirical wavelets. Over 250,000 travel times were picked, from over 1.4 million records, all of which were human-checked for accuracy via a Portable Document Format (PDF) catalog file making system. Many events were specifically selected to bolster southern hemisphere coverage. Coverage maps show that, while the northern hemisphere is more densely sampled, the southern hemisphere coverage is robust. The travel time data set, empirical wavelets, and all measurement metrics are publicly available and well suited for global tomography, as well as forward modeling experiments.

1. Introduction

Freely available global seismic data continue to increase in volume, with data from thousands of seismographic stations available for any given modern earthquake. Data agencies, such as the Incorporated Research Institutions for Seismology (<http://www.iris.edu>), F-net Broadband Seismograph Network (<http://www.fnet.bosai.go.jp>), Northern California Earthquake Data Center (<http://www.ncedc.org>), Canadian National Seismograph Network (<http://www.earthquakescanada.nrcan.gc.ca>), and Observatories & Research Facilities for European Seismology (<https://www.orfeus-eu.org>), are examples of sources of freely available digital waveform data. The growing regional and global seismic data sets afford an increase in sampling coverage of Earth’s mantle and therefore play an important role in Earth structure determination in both forward and inverse studies. For example, seismic body wave travel time information is an essential component of seismic tomography models of global mantle structure (e.g., Durand et al., 2017; Grand, 2002; Houser et al., 2008; Ritsema et al., 2011). We use all freely available data from these networks to construct an up-to-date global travel time data set.

A number of methods can be used to measure seismic travel times for global mantle structure studies. These include picking by hand, such as with many of the travel times in the voluminous International Seismological Centre (ISC) data set, which has been commonly used in *P* wave tomography studies (Inoue et al., 1990; van der Hilst et al., 1997; Woodhouse & Dziewonski, 1984). Handpicking is subject to human error and inconsistencies, and moderate noise levels can erroneously modulate wave onset times. As the sheer volume of data continues to rapidly grow, this approach becomes less and less feasible due to the time-consuming nature of handpicking data. A less subjective approach has been to cross-correlate observed seismic waveforms with synthetic seismograms to obtain travel time residuals (e.g., Houser et al., 2008; Ritsema & van Heijst, 2002; Rost, 2002). This method has the benefit that it can be automated, with signal-to-noise ratio (SNR) considerations incorporated. However, data from any given earthquake can

have variable pulse widths from source directivity and path effects (e.g., attenuation, multipathing, and scattering), so that some level of low-pass filtering is often employed to equalize observed pulse widths. Using longer periods ensures a more consistent match to synthetic reference pulses. Waveform information (and travel times) sensitive to structure at shorter scales is desired but may be subject to variable pulse widths in observations. The body-wave travel time data sets used in seismic tomography models have a wide range, for example, from an upper period limit of ~ 15 s (e.g., 15 s in GyPSuM, Simmons et al., 2010; 15 s in HMSL, Houser et al., 2008; 16 s in S4ORTS, Ritsema et al., 2011; 20 s for S362ANI, Kustowski et al., 2008).

A third method for obtaining travel times involves correlation-based methods between observed phases, like multichannel cross-correlation (Lou et al., 2013; Pavlis & Vernon, 2010; Schaff & Waldhauser, 2005; Vandecar & Crosson, 1990). Users can handpick an onset time in stacks of data made by such correlation schemes (e.g., Lou & van der Lee, 2014) to get absolute time anomalies. These types of algorithms have the benefit of inherently including an averaged source-time function effect from unusual source processes (i.e., effects that synthetic seismogram construction may not have included). However, as with the other methods, an onset time determined from a stack of data inherently averages any timing differences from variability in wave-shape (especially width) due to source directivity, lateral variations in attenuation, and possible multipathing in the presence of strong heterogeneity.

Another approach, which accommodates variable pulse widths and shapes, is cluster analysis which groups distinctly different waveforms. For example, Houser et al. (2008) employed an automated cross-correlation algorithm on all data with high SNR. This process results in a cluster tree from which a cluster level is chosen (to maximize the waveform population and remove poor data) on an event-by-event basis. A user then handpicks an onset time for the average waveform shape of each cluster, using synthetic seismograms as a guide. Thus, this method is a bit of a hybrid of handpicking and multichannel correlative schemes. However, if waveform width is smoothly varying (e.g., from azimuthal dependence of directivity), clustering may blur onset time differences if too few clusters are chosen.

In this study, we present a method that builds an average waveform shape of observed data for the purpose of documenting travel times but with the additional objective of accommodating variable pulse width shape in the data used to make the average shape. This permits the use of a shorter period for the corner of the low-pass filter, thus retaining effects from smaller-scale structural phenomena. We have developed the method with an aim for building a global data set of transversely polarized *S* waves. The following sections present the empirical wavelet (EW) development assumptions and methodology, the global data set, and some basic information about the resulting measured travel times.

2. Global Data Set

2.1. Data Collection

Our goal in this project is to build a global data set of SH wave travel times. To achieve this, we collected all available data from several agencies that freely share data (see Table 1). We initially collected global broadband seismic data for earthquakes in the time period from January 1994 to October 2017, with moment magnitude greater than 6.0 and reported source depth larger than 50 km. The beginning date of 1994 was chosen based on ample digital data available for each event to confidently build EWs, described in the next section. This resulted in 733 deep earthquakes being collected. The source magnitude and depth restrictions were implemented to obtain earthquakes with enough energy to be observed globally and with the depth phases (i.e., upgoing energy from the source that produces surface reflections like sS) arriving later than downward traveling direct waves. All events were inspected for possible contamination from other events which occurred nearby in time. If any energy was apparent, (including from local seismicity), the event was omitted from our catalog (only a small number of events were rejected). Spurious energy was noted as arrivals appearing in data in a systematic fashion (e.g., with distance in record sections or energy localized in time and distance at a very different frequency content). Events with complex source-time functions, either due to very long duration (e.g., from exceptionally large earthquakes) or complex waveforms containing multiple peaks, as well as events with poor SNR (usually less than 2.0), were rejected.

We initially processed every event from 1994 to 2007. To explore path coverage diversity from different station geometries, we processed most events in 2013–2014. It became clear that many events were in regions in

Table 1
Seismic Networks Used in This Study for Global Data Set Construction

Network name	URL
Incorporated Research Institutions for Seismology	http://www.iris.edu
Observatories & Research Facilities for European Seismology	http://www.orfeus-eu.org
Northern California Seismic Network	http://www.ncedc.org/ncsn
F-net Broadband Seismograph Network	http://www.fnet.bosai.go.jp
Canadian National Seismic Network	http://www.earthquakescanada.nrcan.gc.ca/stndon/CNSN-RNSC

Note. Data were collected using software associated with each data center, including Standing Order for Data, Batch Requests, Fast (BREQ_FAST), Networked Data Center Protocol, and AutoDRM (an email-based request tool).

which we already possessed abundant data (e.g., Fiji-Tonga, South America, and northwest Pacific subduction zones). To further optimize global data coverage, a second stage of event collection involved shallow earthquakes with source depth less than 50 km (again with magnitude greater than 6.0). This netted a much larger number of possible events that motivated a prioritization scheme for the shallow events that (a) favored recent time periods (i.e., after 2006, when more network data were available) and (b) ranked events according to the greatest distance from events already processed in our catalog. This insured the most even coverage of earthquakes for any given amount of data processing time devoted to this project. We ended up with 113 shallow events from 1994 to 2017 in our data set culled from roughly 1,400 events; the discarded events were either poor quality (low SNR) or in duplicate locations of other events. These shallow events play an important role in expanding the global coverage provided by the deep earthquakes. We more exhaustively processed some recent year events (e.g., 2017 and all source depths) to ensure possible path coverage improvements from moving network arrays, such as the Transportable Array from EarthScope's USArray (<http://www.usarray.org>, <https://earthquake.usgs.gov>). Maps showing the geographical distribution of earthquakes and seismic stations are presented in Figure 1. Zoom plots illustrate especially dense station distributions in North America, Europe, East-Asia, and the west coast of South America. Our final data set amounted to 360 earthquakes (113 shallow and 247 deep), with recordings from 8,409 unique seismographic station locations.

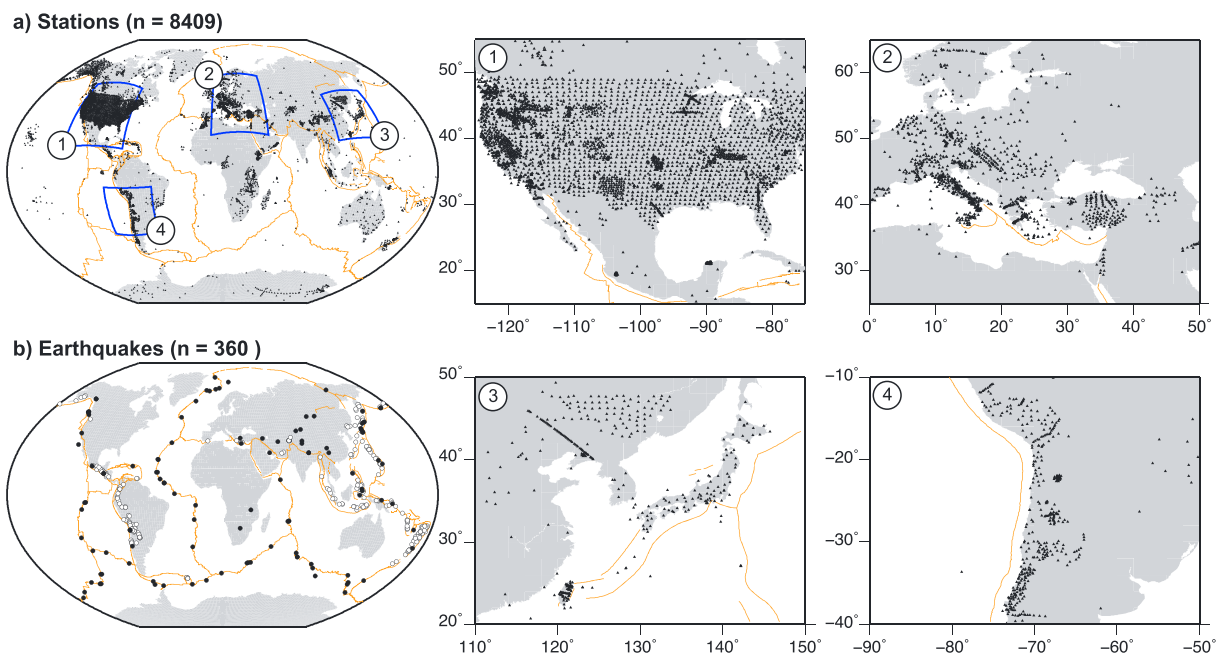


Figure 1. Geographical distribution of (a) stations with four regions (blue boxes) shown enlarged on the right and (b) earthquakes used in this study. The “*n*” value above each map indicates the number of stations (top) or events (bottom). Earthquakes deeper than 50 km are white-filled circles with black outlines; earthquakes shallower than 50 km are solid black circles. Plate boundaries are orange lines. The zoomed in station panels correspond to relatively dense station coverage in the United States (panel 1), Europe (panel 2), Japan and West Asia (panel 3), and western South America (panel 4).

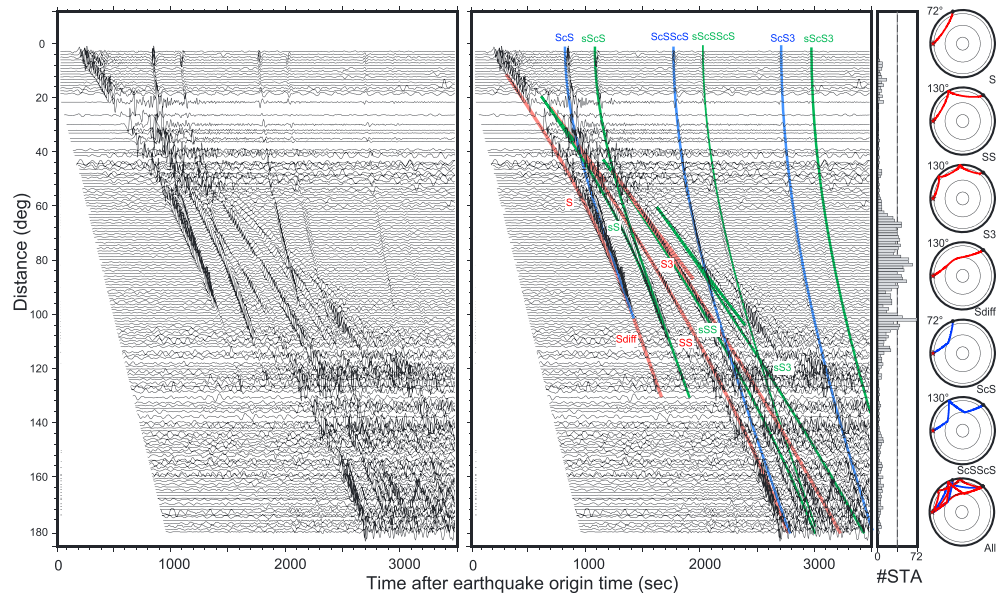


Figure 2. Record section for an event on 28 May 2012 (origin time 05:07, source depth 591.1 km). Nearly an hour of record length is shown for the transverse component of motion velocity recordings; each trace is a stack of all records in a 1.5° distance window. The number of records for each stack is plotted in the histogram to the right. The two record sections are identical, except the one on the right has travel time predictions of S, SS, SSS, and Sdiff (red lines) and the core-reflected ScS, ScSScS, and ScSScSScS waves (blue lines). Green lines correspond to depth phases. The small cross sections to the right display example raypaths of the six main phases used in this study: S, SS, SSS, Sdiff, ScS, and ScSScS. The cross section marked by “All” combines the paths of the six phases.

2.2. Basic Processing

We collected a 2-hr time window length following the earthquake origin time for all available seismic stations (i.e., distances between 0° and 180°), for all events. For each station, three components (north-south, east-west, and up-down) of broadband data are collected, and then the horizontal components were rotated to the great-circle path to obtain the radial (R) and transverse (T) components of motion. Here we focus on the transverse component as our target is SH-polarized S waves. The instrument response for each station was removed through deconvolution using the pole-zero file supplied by the data agency. All data were then band-pass filtered in the period range between 16 and 100 s. The upper filter corner was chosen after trial-and-error experimentation aimed at finding a balance between retaining the shortest periods (which renders some data unusable because of complex higher frequencies) and retaining the largest number of records (which is achieved by stronger low-pass filtering but at a cost of losing unique waveform information at shorter periods).

2.3. Example Event

We show an earthquake that occurred on 28 May 2012 as a representative event to illustrate our main data processing procedures. We first present a full record section profile for roughly an hour of data, over the full distance range (Figure 2). Travel time curves of the key seismic SH phases that are present are also displayed. This event is deep focus (depth of 591.1 km), so many depth phases are readily apparent. Our data collection for this event yielded 2,164 stations, which is too dense to clearly plot; thus, we summed the records every 1.5° in distance (and plot the number of summed records in the small histogram to the right). This event is typical of well recorded earthquakes in that the seismic waves S, SS, SSS, Sdiff, ScS, and ScSScS (see globes to the right in Figure 2) are commonly visible. Thus, in this paper, we focus on these six phases, which provide a relatively good sampling of mantle structure with depth (e.g., see the “All” cross section in Figure 2). ScSScSScS (“ScS3”) is also visible for this event but is less commonly observed across our event collection. In section 3, we introduce our approach for building a representative EW for each event, which then permits us to build our travel time data set for these phases for all our events.

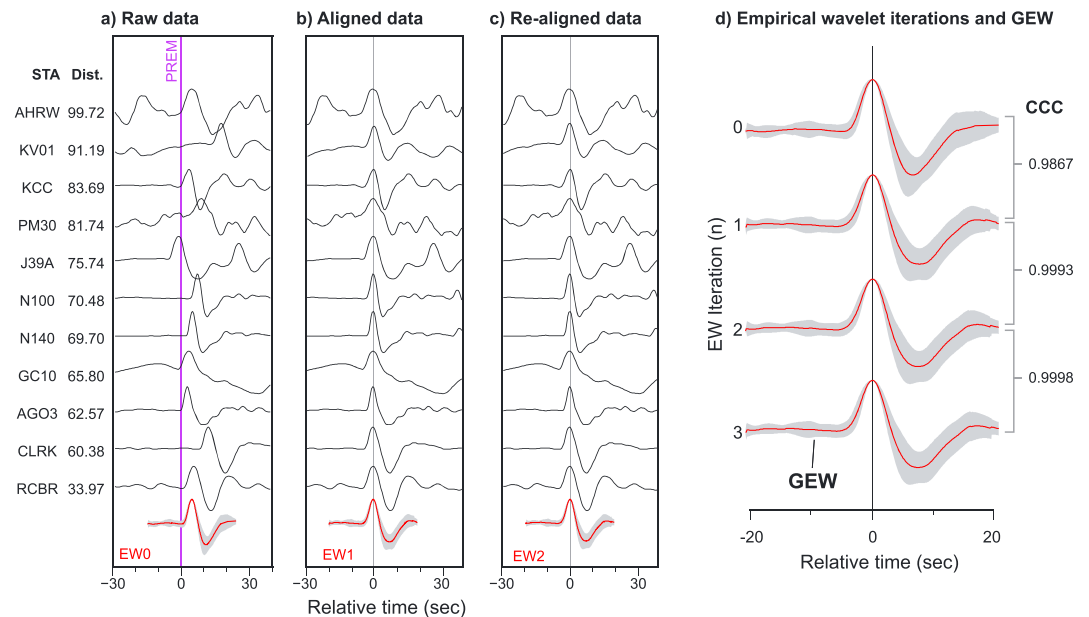


Figure 3. Sample seismograms from the 28 May 2012 event of Figure 2 (station names and epicentral distance in deg given on the left). In all panels the traces are centered on the direct *S* wave, and plotted relative to the *S* wave time predicted by PREM. (a) *S* wave recordings displayed in order of epicentral distance, then directly stacked to generate the zeroth stack, EW0, which is shown at the bottom in red with one standard deviation shown as the gray shaded region. (b) The records from (a) have been aligned with EW0 using cross-correlation and then restacked to make EW1, shown at the bottom. (c) Same as in (b) except the records are now aligned with EW1 and restacked to make an update, EW2, shown at the bottom. This process is repeated until the stack does not update any longer. (d) The empirical wavelet iterations are shown, from EW0 to EW3 (red lines) with one standard deviation (gray shading). The CCC between successive empirical wavelets is shown on the right. The final iteration (EW3 here) is called the GEW. GEW = general empirical wavelet; CCC = cross-correlation coefficient.

3. EW Construction

In this section we introduce our method for building an average shape of the direct *S* wave for each earthquake, which we define generally as “empirical wavelet.” Our approach accommodates the variable pulse width that is present in the data (for every event) and ultimately assigns a travel time for all phases of interest based upon their onset time.

3.1. EW for the Direct *S* Wave

We construct an EW for each event by averaging the shape of all *S* waves at distances greater than 30° , up to the core diffraction distance. The minimum distance is introduced to avoid waveform distortions associated with triplications from the 410- and 660-km discontinuities. We set the maximum distance to be before the onset of core diffraction (as defined by ray theory) to avoid using waves which might be anomalously broadened by the effect of diffraction and/or attenuation (and/or scattering) in the EW construction process. As we introduce the steps of the EW making process, we present a small subset of the records from the earthquake shown in Figure 2 to demonstrate the data processing procedures in a sequence of figures. The steps that follow outline an iterative EW making process which ultimately normalizes pulse widths of records used in the final EW, in order to preserve the onset shape of the records. This refined EW shape is then broadened or narrowed to fit every record in the process of identifying onset times in the data. This process is similar to iterative stacking/alignment methods of past studies (e.g., Pavlis & Vernon, 2010), except our method adjusts pulse widths to optimize the average pulse shape, which we describe below.

3.1.1. Step 1: Construction of the EW0

In our first step, before stacking the data, we calculate the predicted polarity of the *S* wave for every station using the focal mechanism information from the Global CMT database (Dziewonski et al., 1981; Ekström et al., 2012). Any record with a predicted negative polarity is flipped. All records are then normalized with the maximum amplitude set to unity and then stacked within a 40-s time window (40 s for *S* and *ScS*;

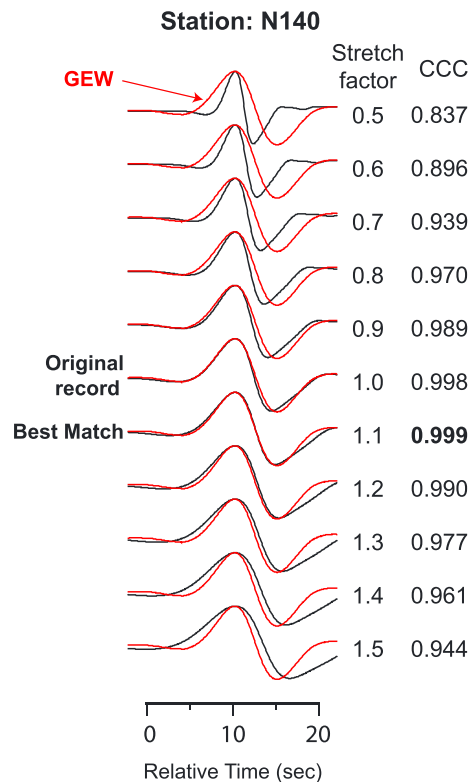


Figure 4. Observed *S* wave pulse from station N140 (of Figure 3) shown with different degrees of time compression/expansion (black traces, original record has stretch factor of 1), each compared with the GEW from Figure 3d (red traces, which are all identical). The stretched record that gives the highest CCC with the GEW (e.g., the bold black “Best Match” trace with stretch factor 1.1) is retained to make the stretched empirical wavelet. The stretching factors and corresponding CCCs are listed on the right side. GEW = general empirical wavelet; CCC = cross-correlation coefficient.

onset time if using correlative algorithms that match the GEW to the data. Here we seek to construct an EW with a sharper onset shape that is more representative of each record’s onset. To achieve this, we apply a wave-shape matching algorithm that matches each record to the GEW for the sake of building a modified EW. Specifically, every record is perturbed in width (by stretching or compressing in time) to best correlate with the GEW. A family of modified records (for each observation) is made ranging from a stretching factor of 0.5 (50% narrower) to 10 (10 times wider) with an interval of 0.01 (thus 950 stretching modifications). The stretched record that produces the maximum correlation with the GEW is retained. This waveform stretching perturbation process to best correlate with the GEW is illustrated in Figure 4, using a record from the population in Figure 3. The best matching stretched record for every observation is then used to make an updated EW. This updated EW, made from stretched records that best correlate with the GEW, better retains wave-shape information, since it minimizes any temporal blurring of the pulse onset. We call this new EW (which is stacked using the same weighting scheme as used in the GEW) the Stretched EW (SEW). A comparison between the GEW and the SEW for the records of Figure 2 is presented in Figure 5. Immediately apparent is the far reduced standard deviation around the SEW on the main up and downswings of the *S* wave. The onset of the wave is sharper and more easily identified. Next, we describe an approach that utilizes the SEW to best match the raw (unaltered and unstretched) seismic waves to determine arrival times.

3.2. Onset Time Determination

The short period end of the period range of our data is 16 s. At this period, variability in waveform pulse width is present. Here we introduce our method of adapting the SEW shape to best fit every record and then to objectively and automatically identify the onset time of the record. We proceed with velocity recordings to

60 sec for all other phases) centered on the Preliminary Reference Earth Model (PREM, Dziewonski & Anderson, 1981) predicted travel time. This initial, Zeroth EW (EW0), stack is an initial estimation of the *S* wave average shape. Figure 3a presents the EW0 construction process for the small subset of records from the event of Figure 2.

3.1.2. Step 2: Iterative EW Updating to Construct the GEW

Once the EW0 estimate is made, the records are shifted to align with EW0 using cross-correlation (Figure 3b). They are then restacked with this new alignment to construct an updated EW (EW1 in this first iteration), where each record is weighted before stacking according to its cross-correlation coefficient (CCC) and its SNR. The SNR is defined as the ratio of the average *S* wave amplitude in the one period time window of the record centered on the PREM predicted time relative to the noise window defined as the average amplitude in an 80-s window that ends 20 s before the predicted *S* wave time. The weighting scheme was constructed to down-weight the influence of anomalous records to the stack, that is, records with high noise level or significant dissimilarity to the stack. In our experience, records with SNR below 2.2 and CCC less than 0.6 are too noisy to confidently identify the phase of interest and are thus excluded in the construction of the EW. The EW construction process is iteratively implemented (e.g., Figures 3a–3c) until the CCC between the previous and current EW is greater than 0.95. The iterative updating of EW is shown in Figure 3d and illustrates the fairly rapid EW evolution to a stable shape. We refer to the final EW (in Figure 3d) as the General EW (GEW).

3.1.3. Step 3: Varying Pulse Width to Construct the SEW

For all earthquakes, seismic wave pulse widths (e.g., for the direct *S* wave) are variable due to source directivity, variable attenuation along different paths, and possible structural effects like multipathing and scattering. However, in the iterative stacking process of step 2, these effects are ignored, and thus records possessing different pulse widths are stacked together. The resulting GEW thus possesses a shape of the onset of the waveform that is an average of variable width waveforms. This smoothing effect will reduce the accuracy and confidence in determination of the

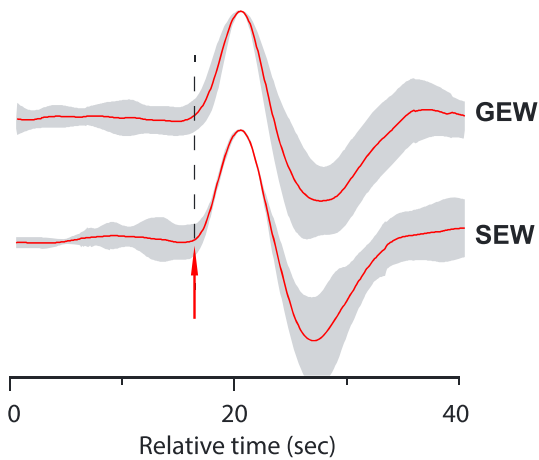


Figure 5. Comparison of the general empirical wavelet (GEW) and stretched empirical wavelet (SEW) for the records of Figure 3. The GEW and SEW are shown as red traces with gray shading representing one standard deviation around the stack. The arrow indicates the onset in the SEW, which is sharper than the more rounded onset in the GEW due to averaging records of variable width. Also apparent in the SEW is the significantly reduced variability around the main upswing and following downswing of the *S* wave.

take advantage of sharper pulse onsets relative to displacement records, which helps to reduce uncertainties. The steps that follow are a continuation of steps 1–3 outlined in the last subsection.

3.2.1. Step 4: SEW Adaptation to Individual Observations

To systemically and objectively identify the onset of each *S* wave, we employ an adaptive waveform fitting technique that finds a perturbation of the SEW width that best fits each record. Since the SEW is roughly the average width of the population of *S* waves for each event, half of the *S* waves will on average be narrower than the SEW, and the other half of the *S* waves will have broader pulse widths. We build a collection of perturbations of the SEW that span the width range from 50% more narrow, up to 10 times broader. The narrowing of the SEW is achieved simply by changing the time spacing between data points and then reinterpolating (i.e., a time compression). To account for a broadened observation relative to the SEW, we convolve the SEW with a series of t^* operators (Futterman, 1962) to simulate the effect of attenuation. We note that we do not incorporate the time shift associated with t^* operators; we simply utilize the wave shape due to the operator. Up to 2,000 width gradations of the SEW are generated for each earthquake and cross-correlated with observed *S* waves to determine the optimal compressed or expanded SEW that fits each record. Figure 6 shows examples of the adaptive waveform fitting approach for narrow and broad records (Figures 6a and 6b, respectively). The SEW better matches the observed waveform after being

adapted to optimally fit. Adapting the SEW to fit observations allows more confident arrival time estimations over the broad range of observed waveform widths.

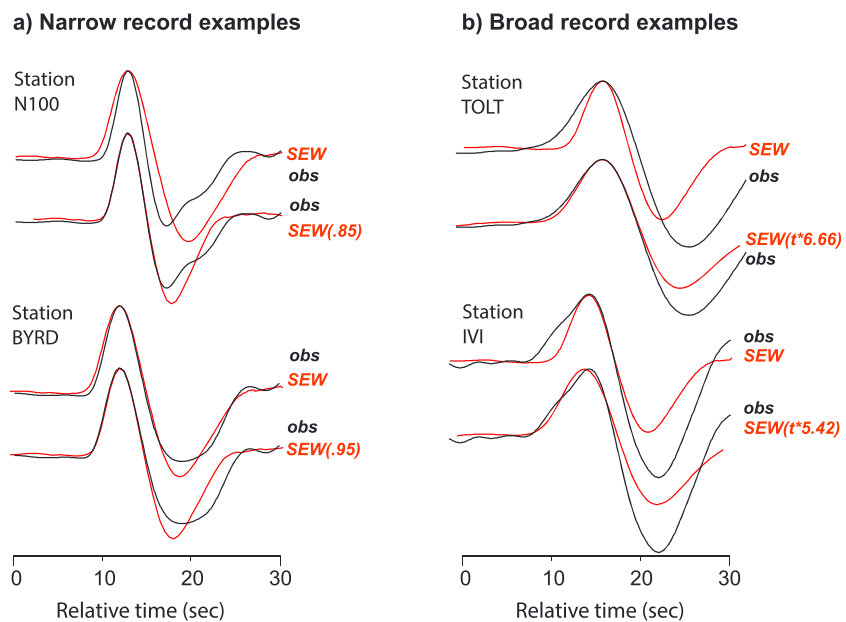


Figure 6. Examples showing the SEW being (a) narrowed and (b) broadened to maximize the correlation with observations from the 28 May 2012 event. (a) Observed *S* waves from stations N100 (top) and BYRD (bottom); black traces are the data, and red traces are the unaltered SEW and the SEW that has been narrowed to best match the observation. The time reduction factor that gives the best fit is shown in parentheses, for example, for station N100 the best-fit SEW has been narrowed to 0.85 its original time width. (b) As in (a) except the observations are broader than the SEW. For these stations, the SEW is convolved with a t^* operator to obtain a best fit with the observation. For the two examples, the t^* value is given in parentheses. The examples in this figure demonstrate the variable pulse widths in the data and how perturbing the SEW can result in matching the observed shapes. SEW = stretched empirical wavelet.

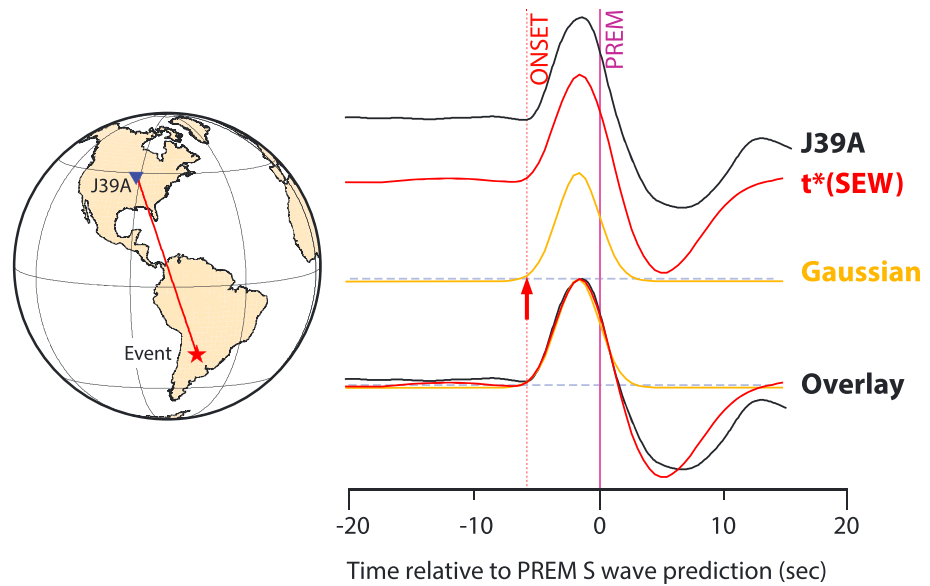


Figure 7. Onset time determination from adapting a Gaussian function (orange trace) to match the SEW (red trace) that best fits the *S* wave observation (black trace) for the deep focus earthquake (red star on globe on left, also, Figure 3) recorded at station J39A (blue triangle in globe). The SEW has been convolved with a t^* operator to best fit the observation. The PREM time for this recording is shown by the purple vertical line. The onset time corresponding to the 1% amplitude level of the Gaussian function is indicated by the red arrow (and vertical red dashed line), which is assigned to the observation. The three traces are overlain in the lower right. This method indicates this record has a travel time anomaly of -6.7 s relative to PREM. SEW = stretched empirical wavelet.

3.2.2. Step 5: Best-Fit Gaussian Functions for Onset Time Determination

Our goal is to determine the onset time of seismic wave arrivals in an automated fashion. After trial and error, we determined that assigning an onset time to a Gaussian function that best reproduces a record's best-fit SEW produces a more stable result (across all data) than assigning an onset time to the SEW (the Gaussian function and factor are defined in section 4.2). Our approach is as follows: (a) determine the Gaussian function width that gives the highest CCC with the SEW (from step 4) for every individual record and (b) define the onset time in the Gaussian function from an empirically determined amplitude level: When the Gaussian peak is set at unity, the onset time is fixed to be where the Gaussian amplitude is 0.01 (i.e., the 1% level) for data that has not significantly broadened. Figure 7 presents an example of this process. If the data are broadened beyond the SEW with a Gaussian factor greater than 30, we increase the amplitude in the Gaussian function which inherits the onset time, resulting in a later onset time assignment. This method minimizes uncertainties associated with differences in amplitudes with SEW onsets from different earthquakes, since the amplitude growth of the Gaussian (from zero) is systematic. Thus, the onset time for every record is automatically assigned in this process. We also experimented with automatically assigning onset times to the SEW. However, the precursory energy leading up to the SEW onset was variable, thus there was not an amplitude level associated the SEW onset that was uniform across the event population. We briefly note that if we carried this process through with the GEW instead of the SEW, all arrival time estimates would be earlier (how much would depend on each event), because the GEW has a smoother, more distributed, onset time (Figure 5). Doing the same procedure with a synthetic seismogram (stretching, onset assignment, etc.) instead of the SEW is possible but does not accommodate possible source time function variability we see for some events.

3.3. Waveform Misfit Measurement

Records with low SNR have less clear waveform onsets. Also, some records may have complex waveforms from multipathing or scattering effects that add wave-shape complexity, such as additional shoulders or double peaks or even precursory energy. The previous steps yield a best-fitting SEW to every *S* wave, for every event that is processed. We thus have a means to document how well each observation compares to the

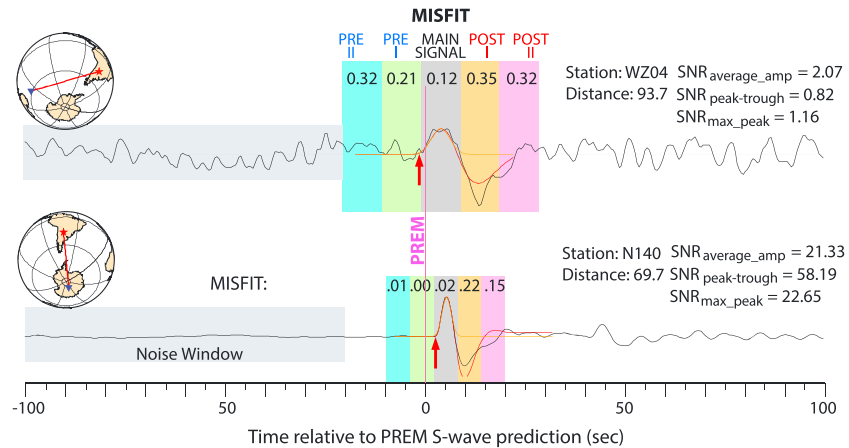


Figure 8. Two example *S* wave records (stations WZ04 and N140) are shown along with misfit and SNR measurement windows and values. These are from the same 28 May 2012 event as in previous figures. The small globes to the left present the event (red star), stations (blue triangles), and great circle paths (red lines). Purple vertical line is the PREM predicted time. Two precursory and postcurcory time windows of one pulse width flank the pulse width of the main signal, where misfit measurements are made (numbers at the top of the colored boxes). The 80-s gray-shaded window on the left is the noise window used to calculate the different SNR measurements, which are listed to the right. See main text for additional details.

adapted SEW shape (and thus a user of the data set can choose to retain or omit data with significant precursory or misfit energy). Here we define a misfit measurement, which documents the average difference between the record and the best-fitting SEW as follows:

$$Misfit = \frac{\sum_{i=1}^n |A_i^{obs} - A_i^{best\ fit\ SEW}|}{n}, \quad (1)$$

where A_i^{obs} and $A_i^{best\ fit\ SEW}$ are the amplitudes of the i th points of the observed record and best fitting SEW, respectively, where the records have been prenormalized to unity at the peak amplitude of the *S* wave. The numerator is thus the summation of the absolute value of the difference between observed and best fit SEW data points, up to the final data point, n . This misfit measurement is made for five unique time windows: over one period of the phase of interest, over the same period length in the window before and after the phase of interest, and over one additional period length before and following the windows surrounding the main phase window. Here a period is defined (on a record to record basis) as the length in time over which the amplitude of the phase of interest exceeds 10% of the peak amplitude of the phase (see Figure 8), and thus n varies from record to record, depending upon pulse width. The central time window is referred to as the main signal window (gray shaded region in Figure 8); the preceding and following windows (“PRE” and “POST,” respectively, in Figure 8) document the misfit over time segments where precursor and postcursor, as well as waveform distortions which may depart from the best-fitting SEW, might be detected. These misfits can also be used in weighting schemes in forward or inverse modeling using the resultant travel times. The *S* waves presented in Figure 8 are both clear and visible, with a relatively small misfit for the *S* wave signal. However, the noise level is clearly higher for the top record (station WZ04), which is apparent in the PRE misfit values (compared to the lower record). Both records have somewhat moderate POST misfit values that are caused by the negative downswing after the *S* wave window that is not represented in the best fitting SEW (see also the large standard deviation in this POST time region in Figure 5). Nonetheless, the stretched SEW fits both records remarkably well, and a confident onset time is achieved. Misfit measurements for the time window following the main phase of interest can be used to hunt for waveforms broadened by multipathing, that is, additional arrivals from reflections or refractions of strong heterogeneity (e.g., Ni & Helmberger, 2003; To et al., 2005).

We have also computed three unique estimations of the SNR of the *S* wave. Our first method is based on the average amplitude over the one period window of the *S* wave divided by the average amplitude of a noise window that precedes the *S* wave:

$$SNR_{\text{average_amp}} = \frac{\{\sum_{i=1}^{n_S} |A_i^S|\} / n_S}{\{\sum_{i=1}^{n_N} |A_i^N|\} / n_N}, \quad (2)$$

where A_i^S and A_i^N are the i th point amplitude of the Signal (“S,” the phase of interest) and Noise (“N”) windows, respectively, and n_S and n_N are the number of points in Signal and Noise windows, respectively. The signal window length is automatically defined as one period, in the same way as with the main phase misfit window, above. The noise window was set at 80 s, initiating 100 s before the PREM predicted onset time. For later arriving phases (e.g., SS and ScS), for some distances and source depths, there are other phases in this noise window (e.g., direct S or depth phases like sS). These are masked out by taking the PREM predicted time for all known “traffic” phases and adding a ± 15 -s time window around those times and only using parts of the noise window around those masked time segments.

The second measure of SNR that we employ documents the maximum peak-to-trough amplitude within one period (where the period, T , is determined as discussed above) for the signal, as well as throughout the 80-s noise window (i.e., the one period peak-to-trough maximum within the noise window is retained). These are then used in the SNR ratio:

$$SNR_{\text{peak_trough}} = \frac{\max_{0 \rightarrow T} [A_{\text{max_peak}}^S - A_{\text{min_trough}}^S]}{\max_{0 \rightarrow T} [A_{\text{max_peak}}^N - A_{\text{min_trough}}^N]}, \quad (3)$$

where the $A_{\text{max_peak}}^S$ and $A_{\text{min_trough}}^S$ are maximum peak and minimum trough amplitudes, respectively, in the signal (S) window (i.e., over 1 period, “0 \rightarrow T”). The denominator is the same, except that the superscript is N, to signify the search for the maximum peak-to-trough within one period over the 80-s noise window.

The third measure of SNR simply compares the maximum positive peak amplitude of the wave of interest (here an S wave, which is predefined to be unity) to the maximum positive peak amplitude in the noise window. This differs from the previous SNR measure in that it is not a peak-to-trough measurement, thus it can document large amplitude offsets over time lengths larger than one period (e.g., long period energy and baseline offsets of the seismogram). It is simply expressed as

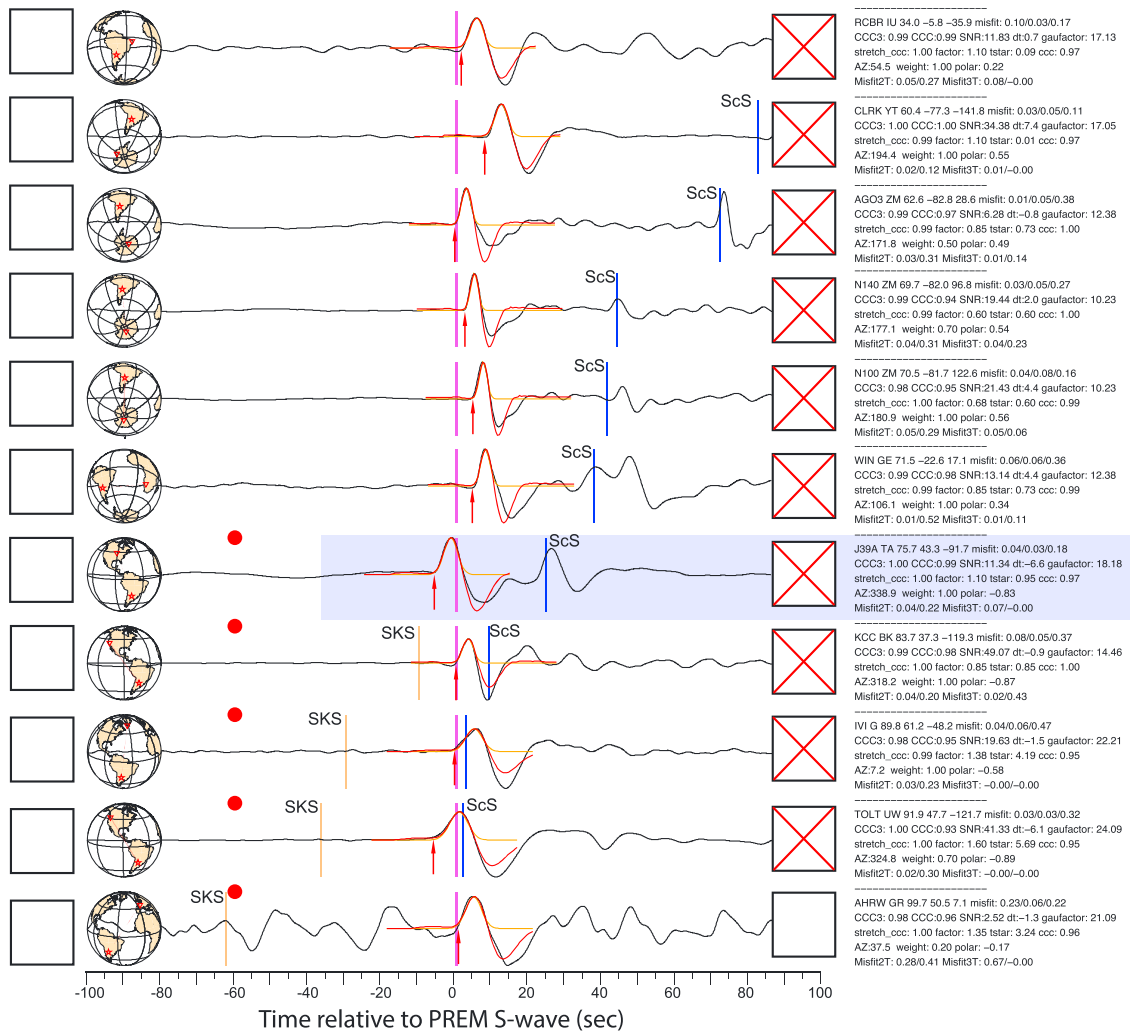
$$SNR_{\text{max_peak}} = \frac{\max_T [A_{\text{max_peak}}^S]}{\max_{N(80 \text{ sec})} [A_{\text{max_peak}}^N]}, \quad (4)$$

where the $A_{\text{max_peak}}^S$ and $A_{\text{max_peak}}^N$ are the maximum peak amplitudes in the signal window (thus, over one period) and the noise window (over the entire 80 s), respectively. The noise time window and all three SNR measures are also presented in Figure 8.

3.4. Data Quality and Catalog PDFs

Here we describe a scheme that automatically classifies each observation as good or poor, and then a PDF file format catalog of the waveforms with the overlain SEW is made for all observations for that event which retains this classification. Ultimately, the PDF is reviewed by humans to either confirm or reject data quality assignments that the algorithm has made. Several factors are used to determine if the records will be automatically characterized as good or poor. They are (a) $SNR_{\text{average_amp}}$: This must be greater than or equal to 2.1 for S and ScS and 2.2 for Sdiff, SS, SSS, and ScSScS to be characterized as good; (b) CCC between the record and its best-fit SEW: This must be greater than or equal to 0.92 to be classified as good for S and ScS and 0.94 for Sdiff, SS, SSS, and ScSScS; (c) onset time anomaly relative to PREM: We require the onset time anomaly be between -15 and $+20$ s to be considered good (though the human reviewer can update the assignment and include larger time anomalies); and (d) interfering seismic waves (traffic): All other seismic waves must be predicted to arrive outside a ± 15 -s window relative to the PREM prediction for the phase of interest for the record to be considered good. If characteristics (a)–(d) are all met, then in the PDF, the data are noted as good by using a box with a red “X” in the box, while data that do not meet these values have the box unchecked (in a PDF business form fashion). Figure 9 shows an example of part of a PDF page that shows the original records, globes to the left displaying path geometry, the best-fit SEW and Gaussian, the onset pick, and many data characteristics

a) Catalog Plot Example for Phase S



b) Station J39A

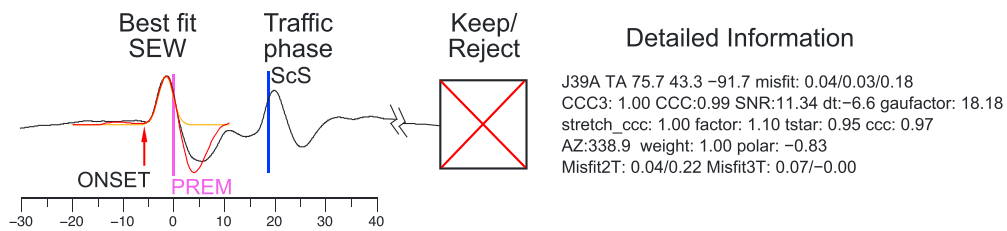


Figure 9. Example of portion of catalog PDF page of direct *S* waves with overlain SEW used for human reviewing. These data are from an event on 28 May 2012. (a) A portion of the PDF page that shows from left to right: an alphanumeric text input box for the user to add a code or time shift if desired/necessary; a small globe showing the event (star)-to-station (triangle) geometry; 200 s of the observed transverse component velocity recording with the *S* wave near zero time, aligned according to the PREM prediction (purple line at zero); a box with a red “X” (or empty) which logs the algorithm’s decision for the data being good or poor, which the reviewer can update, and a text block with information about the station and all the measurements made. (b) A zoom in of one of the records (station J39A, shaded region in top panel), which shows the best-fit SEW overlaid on the *S* wave (red trace), the best-fit Gaussian (orange trace), travel time predictions of other phases (here ScS is present), a red dot that indicates the code flipped the polarity so that the phase of interest is a positive pulse in the plot so all polarities are uniform, the onset time determined from the Gaussian (red arrow), the PREM predicted time (purple line), the retain/reject box, and the detailed information block, with detailed measurements such as travel time anomaly, SNR, CCC, misfit, and Gaussian factor. SEW = stretched empirical wavelet.

printed to the right, along with the boxes which are checked if the code characterized the records as “good.” The viewer of the PDF can then uncheck or check records based on whether or not records are well classified. We found this an efficient means to review every single seismogram in our data set. The above values were chosen empirically after many trial and error efforts at effectively picking onsets on broadband velocity SH data in our band-pass filter (16–100 s). For the 360 events in our data set, this human viewing/rechecking process took roughly 10 months.

A few additional procedures were included in the making of PDF catalogs. The predicted polarities of our phases of interest (S, SS, SSS, Sdiff, ScS, and ScSScS) were computed using the Global CMT catalog (<http://www.globalcmt.org>). If the radiation pattern prediction for any of our observations was in the -0.15 to 0.15 range (where maximum radiation pattern values are ± 1.0), we colored the record purple in our plots. The record was also flipped in polarity and colored green. The algorithm fits a best-fitting SEW to each polarity of the record, so the reviewer of the data has flexibility to choose the flipped polarity version in case the radiation pattern prediction is incorrect. The PDF catalog checked the good box for the best version of the two records, if conditions (a) through (d), above, were met. This procedure was motivated by the observation that phases near the nodes of the radiation pattern are sometimes flipped from the CMT solution for the 10-s period data. This approach was flexible, and the reviewer could easily reject or modify the code's choice, if necessary. Furthermore, records with predicted low amplitude were only retained if waveform behavior was similar to records with predicted higher amplitudes. The PDF displays all records with the phase of interest having the same polarity (up), and a red dot indicates if a polarity has been flipped for plotting purposes. We plot all predicted arrival times of traffic energy, so the reviewer can modify the code's choices if necessary, since some phases of interest may have travel time anomalies greater than our ± 15 -s window used in (d), above, and interfere with traffic energy. As apparent in Figure 9, viewing all records from a given earthquake and a given phase at the same time is powerful—the reviewer can identify if a phase is robust (whether it be the phase of interest or traffic), by viewing near neighbor stations plotted in the PDF near the record being viewed.

In some cases, the best-fit SEW is well matched to the waveform for the phase of interest, but the onset time that is automatically determined does not capture the onset of the observed pulse. This can happen if the wave has experienced multipathing and the front part of the wave has pulled out in front of the SEW; this will result in the assigned Gaussian-derived onset time being in error. The PDF catalog includes a numerical entry box to the left of every trace, where the reviewer can zoom into the observed wave and SEW overlay, determine a time shift, and then enter the time shift value into the number entry box. For all observed occurrences of this type of wave behavior, we applied corrections, so the reported onset times correspond to the actual wave onsets. Once PDF files were saved and closed, we algorithmically extracted information on all selected records from the PDF file.

The EW algorithm and classification approach described above has worked well with most earthquakes and the six seismic phases studied here. However, a small percentage of records experience phase misidentification or false classification (i.e., the SEW gets aligned with a noise pulse). For this reason, the PDF catalog approach with human reviewing was necessary to ensure the highest quality standards. In our quality control process, the reasons we rejected records were that the phase of interest (a) did not have a clear wave onset; (b) had unexpected large precursory energy immediately preceding the wave onset; (c) had nearby unidentifiable large pulses (i.e., ± 100 s around the phase of interest), which puts the source of the wave interpreted as the phase of interest in question; (d) has relatively low amplitude compared to the background noise level; and (e) has interfering (traffic) phases within 15 s of its predicted arrival time. Some events were rejected if their source-time function shape was too complex to be fit with a Gaussian (step 5, section 3.2), which would yield erroneous onset times in our procedure.

Of the ~ 1.4 million records processed, the human checking of the algorithm picks resulted in $\sim 5\%$ of originally rejected picks being added back to the retained data and $\sim 27\%$ of the originally retained data to be rejected. Many good data were rejected by the algorithm based on our SNR criteria (commonly due to some long period energy far ahead of the phase of interest). Some data that the algorithm selected were subsequently rejected because the onset time was unclear, or in some cases, the algorithm selected a noise peak. Thus, the human reviewing part of this work was important in catching erroneous results from an automated procedure.

3.5. EW of Other S Phases

The first arriving shear wave is the direct S. It possesses the largest SNR and wave-shape stability, and thus the direct S is the wave most representative of the source time function of each event. We thus use the SEW from direct S as our reference shape in determination of arrival time, wave shape broadening, and misfit of the other phases (SS, SSS, ScS, ScSScS, and Sdiff). The travel time determination of these other phases is the same as for S, namely, we follow steps 4 and 5 of section 3.2 to determine onset times; we follow section 3.3 to estimate misfits and SNR values; and we follow section 3.4 to construct PDF catalogs for human reviewing of the automatic picking choices made by the algorithm. We note that SS is a minmax phase with a $\frac{\pi}{2}$ phase shift relative to direct S (Butler, 1979; Choy & Richards, 1975). Here we Hilbert transform SS back to the same phase as S (thus, a $\frac{3\pi}{2}$ phase shift). Also, SSS is phase shifted $\frac{\pi}{2}$ beyond the phase of SS, thus a π phase shift beyond S. We similarly put the SSS wave into the phase of S. This allows us to employ the robust SEW created from the direct S for analyses of SS and SSS waves. Figure 10 presents examples from three earthquakes, where the SEW constructed from the S wave was adapted to the phase shifted SS and SSS, as well as Sdiff, ScS, and ScSScS. For each event, 10 records are shown for each phase. We note that our algorithm did not select data for shallow events if the depth phase was expected to interfere with the phase of interest. The human inspection phase of measurements allowed flexibility for omitting or keeping data picks, based on the depth phase behavior.

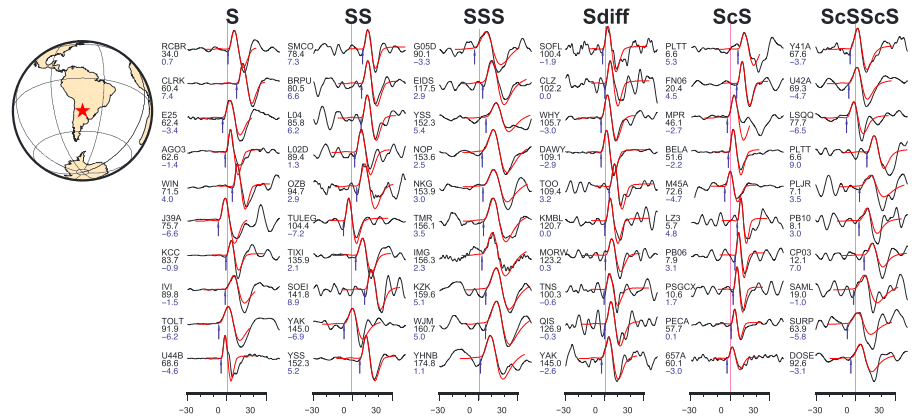
Adapting the direct S wave SEW to fit all the other phases has several practical advantages over developing a separate SEW from each phase of interest. First, the direct S has a better SNR compared to all later arriving phases and is easier to detect since it is a first arriving wave on the transverse component of motion. Also, as we describe in the next section, for any earthquake, usable S waves are far more abundant than the later arriving phases, thus more records are used in the SEW stack. Thus, the Swave-generated SEW stacks are more robust. However, as a postprocessing step to measuring all phases with a direct Swave-generated SEW, it is a simple step to construct SEWs using the other phases (SS, SSS, Sdiff, ScS, and ScSScS) since the good data have already been identified for these later arriving waves. In Figure 11, we present the GEW for each of the six phases (left column of each panel) along with the standard deviation. A general (and expected) trend is that the higher S multiple phases have broadened GEWs due to the effects of the attenuating mantle. However, this trend is not obvious with all stacks, especially those with very few records in the stack. The column on the right for each event presents the SEW for each phase that was constructed by using the Swave-generated GEW for aligning and shape adapting the later arriving phases before stacking. As expected, this results in all SEWs having the pulse width of the starting S wave GEW. By adapting the later arriving phases to the direct S wave SEW, the onsets are generally sharpened, and the standard deviation is reduced near the wave's onset, as well as over most of the first period of the wave. We thus retain travel times for all phases using the S wave SEW due to its increased stability and well-defined wave onset.

4. Results: Travel Times and Other Measurements

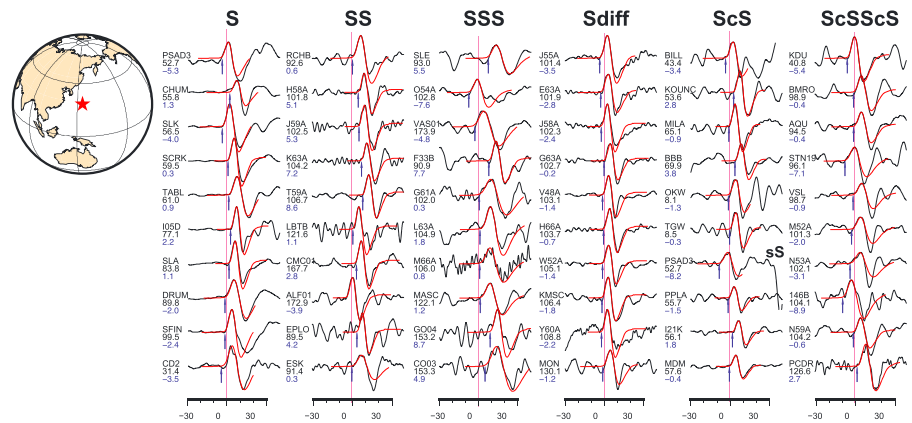
4.1. Number of Measurements

For the S, SS, SSS, Sdiff, ScS, and ScSScS phases we have processed and viewed, over 1.4 million unique seismograms were visually inspected (via the algorithm generated PDF files) from the 360 events. Of these, over 250,000 high quality travel times were retained. The number of retained travel time picks for each phase are given in Table 2, along with the number of records viewed and the percentage of viewed records that are retained. The direct S wave by far has the highest rate of measurement success (56.8%), followed by Sdiff (19.4%) and SS (17.0%). The most viewed phase was ScSScS (with 393,947 records viewed), since it was investigated from 0° in distance to 160° . However, ScSScS only returned confident measurements $\sim 2.6\%$ of the time. The main reasons for records being discarded were low SNR and interference with other phases. The percentage of records measured depends on a number of factors, including event size and radiation pattern combined with event location, the latter which may or may not have stations available at the accepted distance range of the phase of interest. Ridge events in the southern hemisphere were typically noisier than average but used for coverage purposes. Strong deep focus events commonly had more successful picks than average. The direct S wave measurement success varied from less than 1% (for a very noisy southern hemisphere ridge event) to $\sim 89\%$ (for a particularly impulsive and clean South American subduction zone event).

a) Event: 201205280507



b) Event: 201506231218



c) Event: 201505191525

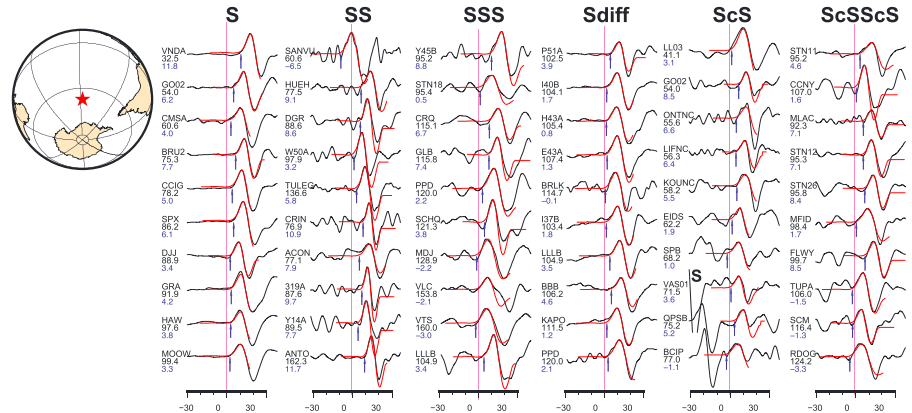


Figure 10. Example records of S, SS, SSS (where SS and SSS are put into the phase of S), Sdiff, ScS, and ScSScS for three events. (a) Event 201205280507 (where the title is in the form $yyymmddhhss$, where $yyyy$ = year, mm = month, dd = day, hh = hour, and ss = seconds of the origin time), with latitude, longitude, depth, and moment magnitude of $[-28.02^\circ, -53.11^\circ, 591.1 \text{ km}, 6.7]$. The globe to the left shows the event location (red star). (b) As in (a) except for event 201506231218, with latitude, longitude, depth, and moment magnitude of $[27.74^\circ, 139.72^\circ, 460 \text{ km}, 6.5]$. (c) As in (a) except for event 201505191525 with latitude, longitude, depth, and moment magnitude of $[-54.33^\circ, -132.16^\circ, 7.2 \text{ km}, 6.7]$. Black traces are the raw records displayed relative to the PREM predicted time and arranged according to increasing distance. The red traces correspond to the S wave SEW for each event, adapted to best-fit every arrival, and overlaid with each phase. The blue arrows correspond to the solution onset times, derived from the best-fitting Gaussian (not shown) to each SEW. The station name for each record is listed on the left and underlain by the epicentral distance and travel time anomaly relative to PREM (blue text). Some additional arrivals are present for some records, and the known phases are named.

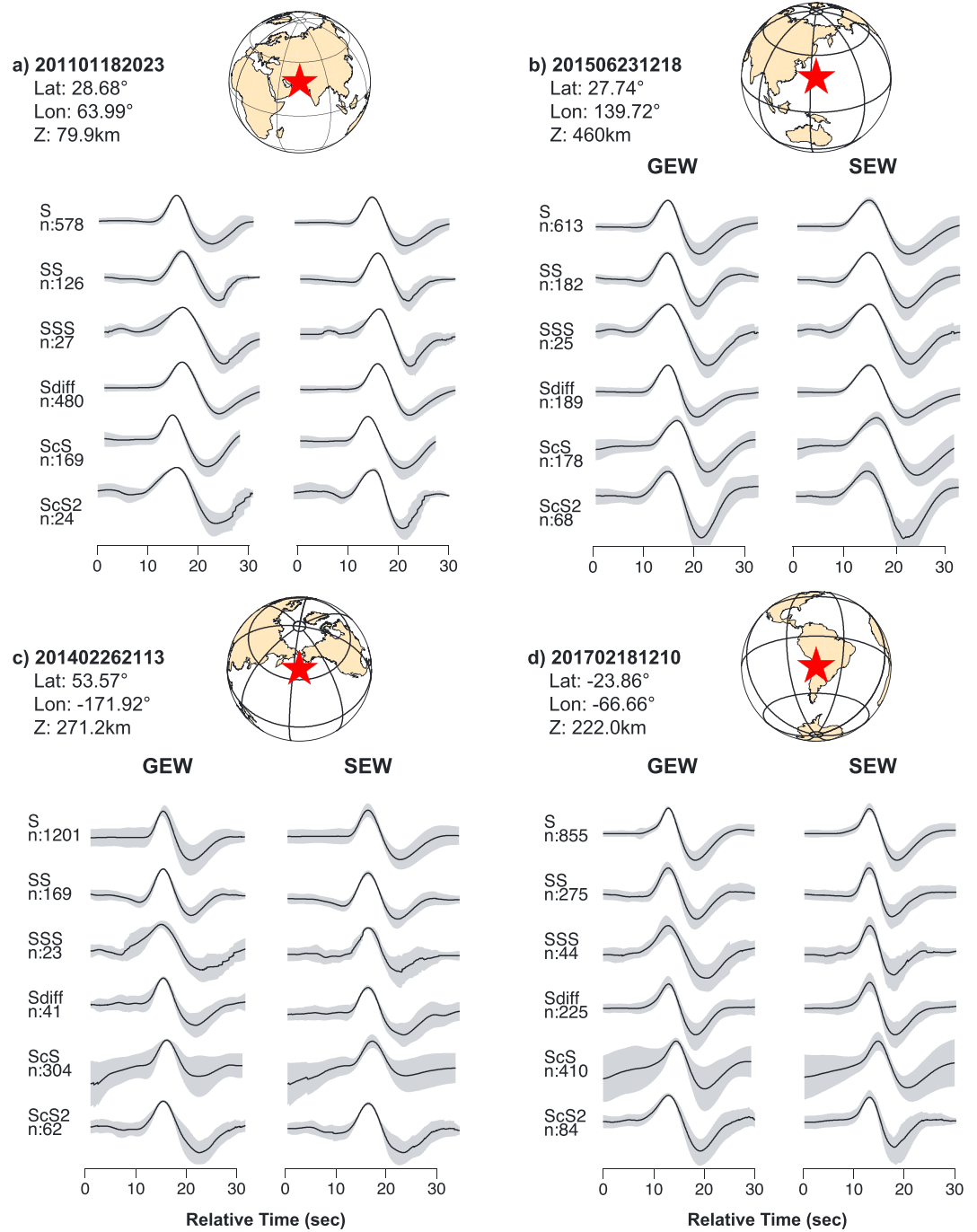


Figure 11. GEW and SEW with standard deviation for four example events in panels (a) through (d), for the seismic phases S, SS, SSS, Sdiff, ScS, and ScSScS, where SS and SSS have been Hilbert transformed back into the phase of S. Also shown are the event date and origin time (in format YYYYMMDDMMSS, see Figure 10), latitude (Lat), longitude (Lon), and source depth (Z), and the location of each event (red star) in a small global map in the upper left of each panel. Each panel has two columns: The left column presents the GEW (along with one standard deviation, gray shading) made from stacking that phase (the phase name is noted on the left, along with number of records used in the stack). The right column is the SEW stack of each phase, using the S wave GEW (top trace in left column) as the reference shape to which records of each phase are adapted to (see text for more details). GEW = generic empirical wavelet; SEW = stretched empirical wavelet.

Table 2
Total Number of Travel Time Measurements in This Study for All Events, Along With the Total Number of Records Viewed and Inspected, and the Percent of the Viewed Data That Produced Successful Travel Time Measurements

Phase name	# Accepted	# Inspected	% Data Accepted
S	123,946	218,094	56.8
SS	53,505	314,259	17.0
SSS	11,927	207,429	5.7
Sdiff	28,499	146,561	19.4
ScS	23,758	158,850	14.9
ScSScS	10,303	393,947	2.6
All	251,939	1,439,140	17.5

4.2. Basic Data Set Attributes

We present some basic attributes of the measurements for each of the six phases in Figure 12. The first column displays travel time histograms for the entire data set. Here we see that the multiple *S* waves (especially SSS) have a greater spread in the travel time anomalies, as would be expected for a wave with proportionally more of its path in the heterogeneous uppermost mantle. The second column presents histograms of the CCCs between observations and the best-fit SEW. Immediately apparent is that the direct *S* wave has very high CCCs without much spread. Phases with the longest paths have a greater spread in their CCCs (viz., SSS and ScSScS). The SNR measurements (from the average amplitude method) are shown in the third column and emphasize the direct *S* wave routinely has the highest measured SNRs. We also present a factor used in

the Gaussian function (fourth column) that corresponds to pulse width. A Gaussian function, G , can be defined as

$$G(i) = e^{-\frac{i^2}{2g^2}}, \quad (5)$$

where i is the number of time points (and thus the length of the function in time points), g is the Gaussian factor (which corresponds to the standard deviation of the function), and e is Euler's number. The Gaussian factor histograms display the clearest evidence for the broadening of data pulses for the longer multibounce phases (e.g., see SSS compared to SS compared to S and ScSScS compared to ScS).

4.3. Empirical Comprehensive Weight

We have computed an empirical weight measurement for all measured data (for all six seismic phases) that incorporates the SNR (average amplitude method), the CCC between the observation and the best

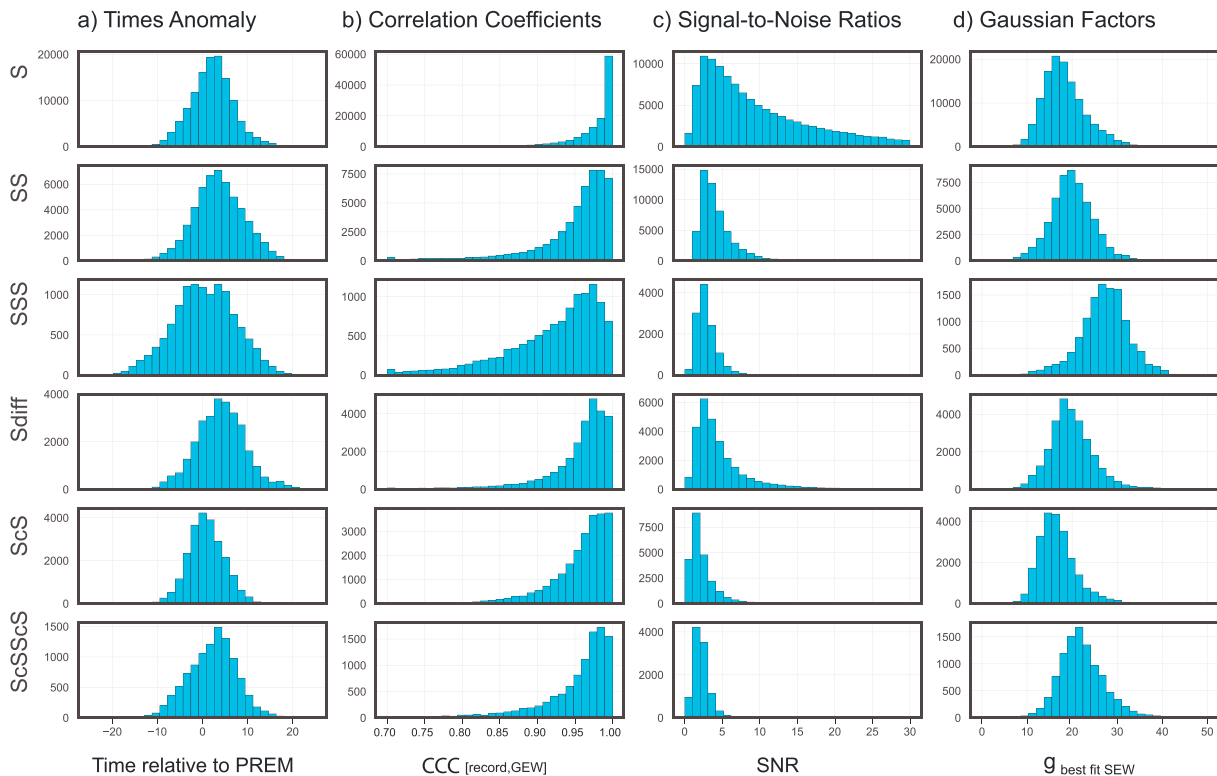


Figure 12. For the six phases studied, histograms are shown for (a) travel time anomaly relative to PREM predictions, (b) cross-correlation coefficients between the phase of interest and the best-fitting stretched empirical wavelet, (c) the SNR measured from the average amplitude method, and (d) the Gaussian factors for the Gaussian function that best matches the stretched empirical wavelet which fits each record. GEW = generic empirical wavelet.

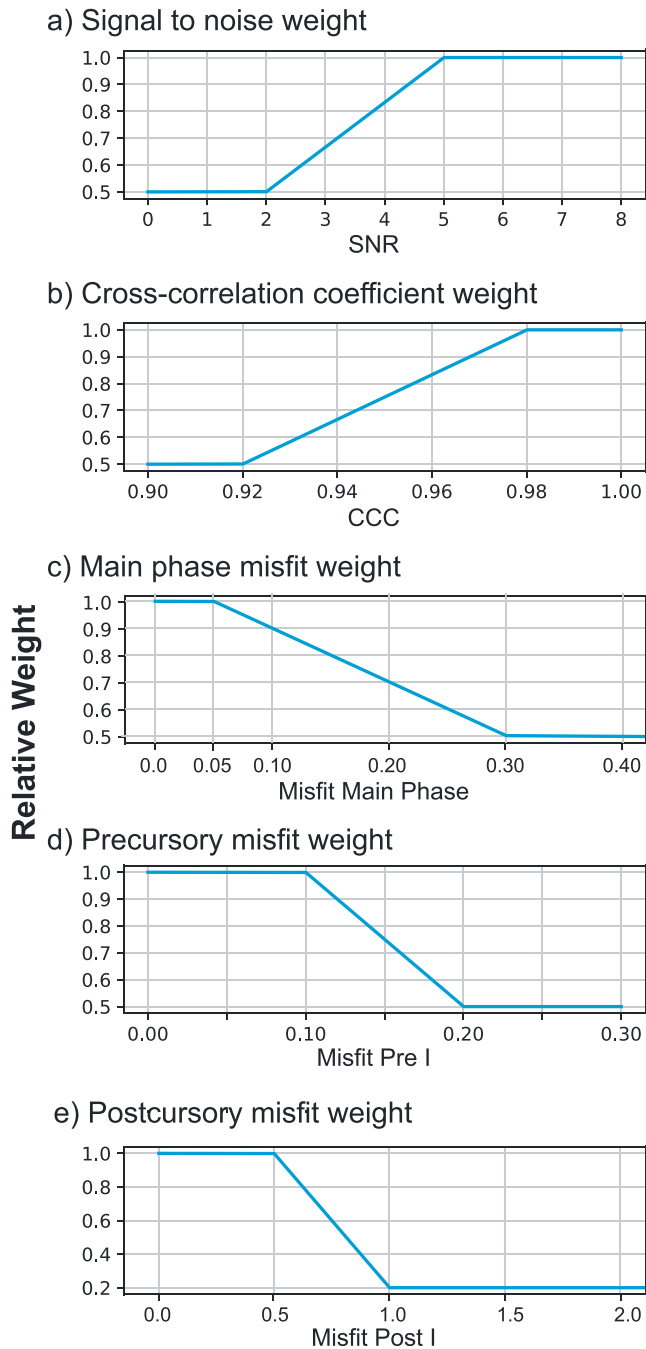


Figure 13. Weighting functions for various measurements made in our data analyses: (a) SNR measured by the average amplitude method (equation (2)); (b) CCC between the best-fitting SEW and the observation; (c) the misfit measured over the pulse width of the main phase of interest; (d) misfit measured over one pulse width before the arrival of the main phase, that is, the precursory energy window (“Misfit Pre I” in Figure 8); and (e) the misfit measured over one pulse width after the main phase (“Misfit Post I” in Figure 8).

fitting SEW, the misfit of the signal to the best fitting SEW over the first precursory one-period length, the misfit of the signal over the main phase, and the misfit of the signal over the first postcursor one-period length. While empirical, we have found that data with SNR greater than 5 are the best quality, and typically diminish in quality for lower SNR values down to 2, below which we set at a constant value of 0.5. In a similar fashion, the CCC’s between observations and the best-fit SEW above 0.92 are common for the good data. This CCC is computed over one period of the main phase (as in Figure 8). For this and other measures of quality, we present weight functions in Figure 14. In addition to SNR and CCC, we show a weight function for the Misfit, measured over a one-period long precursory window (“Misfit Pre I” in Figure 8) and a one-period long postcursor window (“Misfit Post I” in Figure 8), which documents both precursory and postcursor energy. Misfit is also measured over one-period of the main phase (“Misfit Main Phase” in Figure 8). The weighting values are chosen to emphasize the best measurements based on an inspection across the data set during data viewing, as well as looking at the trends in Figure 12. No weight value drops to zero for our data because all data are human viewed, and only chosen if the data were good quality. We define a comprehensive weight for every travel time measurement from a product of the individual computed weights for each record:

$$w_{\text{comprehensive}} = w_{\text{SNR}} \times w_{\text{CCC}} \times w_{\text{misfit_pre_I}} \times w_{\text{misfit_post_I}} \times w_{\text{misfit_main_phase}}, \quad (6)$$

where these weights directly correspond to the panels in Figure 13. This comprehensive weight is presented with the travel times in the tables that can be downloaded from this work. This comprehensive weight number can be used in modeling experiments for simple weighting approaches or the individual weights or raw SNR, CCC, and misfits can be used, if preferred.

4.4. Full Data Set Attributes

In this study we have measured over two decades of data, built travel time data sets of six dominant SH waves, and measured many attributes of the data. The results are available electronically as a supplement to this paper (see Acknowledgments). Table 3 lists all of the assembled information. In addition to the travel time anomalies, many data attributes that relate to pulse width (stretching factor, t^* , and Gaussian factor), quality (SNR, CCC, and misfit), and pulse polarity are given along with event and station information. This information can be utilized in either forward or inverse modeling experiments or used to retrieve the exact parts of waveforms from the data containing phases of interest. We also estimate the period of every measured phase from displacement recordings. However, there is some scatter in the estimations due to the presence of longer period energy in displacement components. To help document possible poor period estimates, we compute a best-fit line to our velocity pulse width measurements (i.e., the difference between the pulse end and start, entries 20 and 19, respectively, in Table 3) plotted against our estimates of period on displacement recordings.

One, two, and three standard deviations relative to this best-fit line are computed. We note if the period estimate is an outlier or not by presenting the standard deviation level in Table 3 (entry 39).

Table 3

List of Data Attributes Compiled and Computed in This Study That Are Shared in Archived Data File (see Acknowledgments)

#	Information	Description
1	Station name	The 3–5 character station name code
2	Network name	The two-digit code for the seismographic network
3	Distance	Epicentral distance between earthquake and station in degrees
4	Station latitude	Station location latitude in degrees ^a
5	Station longitude	Station location longitude in degrees ^a
6	Event latitude	Earthquake hypocentral location latitude in degrees ^b
7	Event longitude	Earthquake hypocentral location longitude in degrees ^b
8	Event depth	Earthquake hypocentral location depth in square kilometers
9	Event magnitude	Earthquake moment magnitude ^b
10	Origin time	Earthquake origin time ^b
11	Azimuth	Azimuth from earthquake to station (in degrees)
12	Back azimuth	Back azimuth measured at station clockwise back to earthquake (in degrees)
13	Phase name	Either S, SS, SSS, Sdiff, ScS, or ScSScS
14	Measured time	Travel time anomaly of phase onset relative to PREM (observed minus PREM)
15	Predicted time	Travel time prediction of the PREM model
16	Amplitude	Amplitude of the peak of the phase, on instrument-deconvolved velocity recordings
17	Radiation pattern	The predicted amplitude between [−1,1] using the SH radiation pattern
18	Flipped polarity flag	Record was modeled after flipping the record's polarity (which was explored for a low radiation pattern amplitude range [−0.15,0.15]), flagged as 0 if radiation pattern prediction is correct, otherwise 1
19	Phase start	The start time, relative to PREM prediction, of the beginning of the time window used to define one pulse width of the phase on velocity recordings, measured at the 10% amplitude level preceding the wave peak (used to auto-define the Misfit measurement windows)
20	Phase end	The end time, relative to the PREM prediction, of the end of the time window used to define one pulse width of the phase on velocity recordings, measured at the 10% amplitude level following the wave peak (used to auto-define the Misfit measurement windows)
21	SNR _{average_amp}	The signal-to-noise measurement from the average amplitude of the signal to the average amplitude of the noise, as in equation (2)
22	SNR _{peak-trough}	The signal-to-noise measurement from the maximum peak-to-trough measurement within one period of the signal compared to noise, as in equation (3)
23	SNR _{max_peak}	The signal-to-noise measurement from the maximum peak in the signal window compared to the maximum peak in the entire noise window, as in equation (4)
24	Misfit _{SIGNAL}	The average difference between the phase and the best-fit SEW over one period (see equation (1))
25	Misfit _{PRE}	As above, except over one period preceding the phase
26	Misfit _{POST}	As above, except over one period following the phase
27	Misfit _{PRE_2T}	As above, except over one period preceding Misfit _{PRE}
28	Misfit _{POST_2T}	As above, except over one period following Misfit _{POST}
29	t^*	The best-fit t^* value that, when convolved with the SEW, gives the best fit to records that are broader than the SEW
30	Stretch factor	A measure of the amount the SEW has to be narrowed to fit records that are narrower than the SEW
31	CCC _[rec,SEW]	Cross-correlation coefficient between observed record and the best-fitting SEW adapted to the record
32	CCC _[rec,GEW]	Cross-correlation coefficient between observed record and GEW, which measures the record's fit to the average phase shape for the event
33	$g_{\text{best-fit_SEW}}$	Gaussian factor of the best-fitting Gaussian function (equation (5)) to a record's best-fitting SEW
34	$g_{\text{event_SEW}}$	Gaussian factor of the best-fitting Gaussian function (equation (5)) to the S wave SEW for the event (i.e., unstretched, un- t^* ed, as in step 3, section 3.1)
35	Misfit _g	The misfit measured between $g_{\text{best-fit_SEW}}$ and $g_{\text{event_SEW}}$ (computed as in equation (1)) which provides a different measure of record broadening
36	$w_{\text{comprehensive}}$	An empirical comprehensive weight value for each data (see equation (6))
37	Noise window traffic flag	Records that have “traffic” (other seismic waves) predicted to arrive in the noise window (of the SNR measurement) are flagged as 1, otherwise 0
38	Period	Estimated period of the phase, from the start and end of the pulse measured at 0.1 amplitude (when peak is set to 1) measured on displacement recordings
39	Period flag	“1” if period measurement is within 1 standard deviation from best-fit line of displacement period and velocity pulse width measurements, “2” if period measurement is in the 1 to 2 standard deviation population, and “3” if in the population greater than standard deviation of 2

Note. The number in the first column of the table below corresponds to the column number in the archived data file. GEW = general empirical wavelet; SEW = stretched empirical wavelet.

^aAs provided by the data agencies in Table 1. ^bAs provided by International Seismological Center.

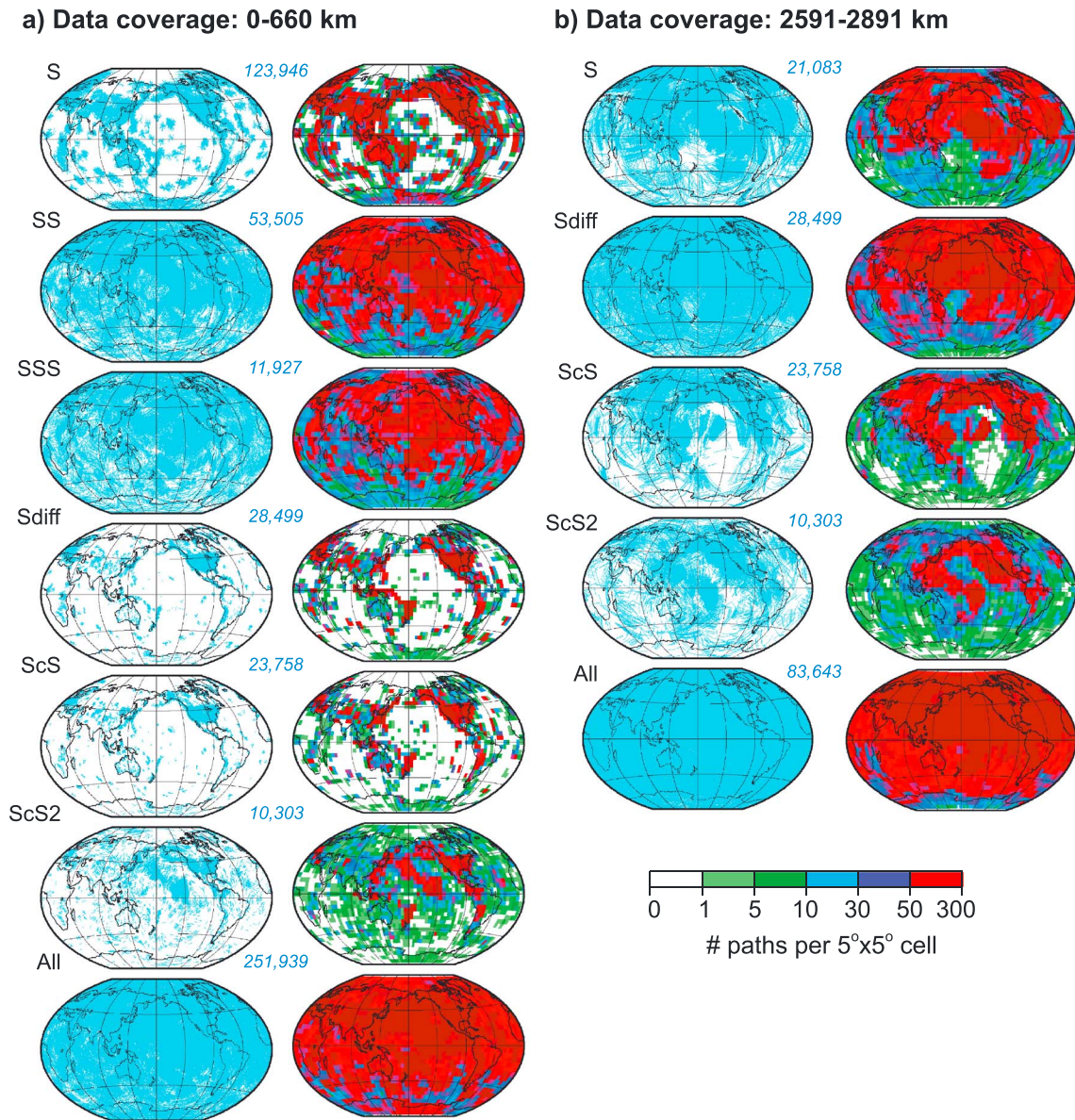


Figure 14. (a) Raypath coverage map in the upper mantle (0–660 km) for the six seismic phases studied here; the upper mantle portion of every raypath is drawn as a light blue line (left column). The panel at the bottom named “All” has all raypaths plotted on the same panel. The right column shows the ray path sampling density in 5° by 5° cells. Red corresponds to high sampling density (see scale bar). (b) As in (a) except for the deepest 300 km of the mantle, the D” layer. Only phases with robust D” sampling are shown. As with (a), the “All” panel combines the D” sampling waves.

4.5. Geographical Sampling Coverage

Geographical coverage and sampling density are important, since they directly relate to model resolution in both forward and inverse approaches aimed at structure determination. However, due to the geographically restricted earthquake-station geometries, the mantle is unevenly sampled. Most of the earthquakes in our data set are located on plate boundaries, especially around the circum-Pacific; a majority of the seismic stations are located on continents in the northern hemisphere, including North America, Asia, and Europe. Therefore, the northern hemisphere is much better sampled than the southern hemisphere. Our event ranking algorithm has helped to bolster path coverage in less sampled event-station corridors, but uneven sampling persists. Figure 14 presents raypath coverage maps of the upper mantle (0–660-km depth) and lowermost mantle (deepest 300 km of the mantle, i.e., the D” layer). Coverage is shown for the individual phases as well as all the phases together. As expected, the northern hemisphere is better sampled than the

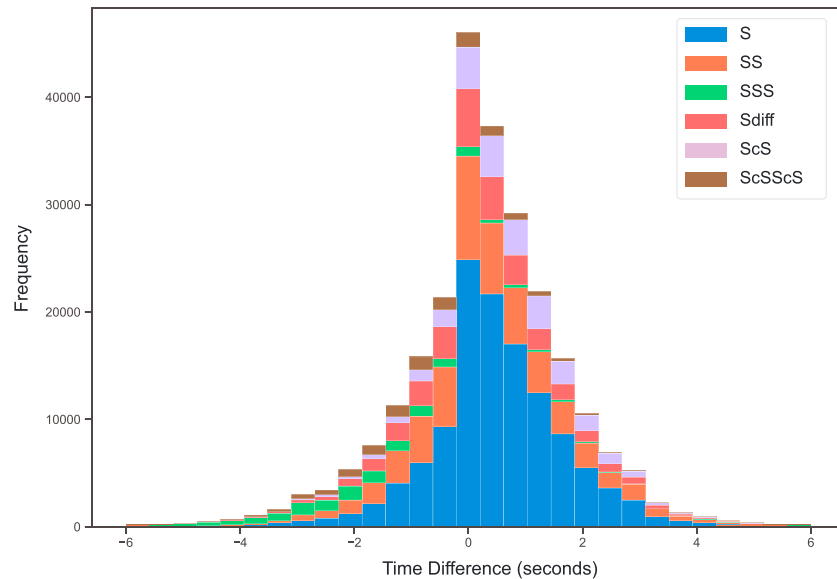


Figure 15. Stacked histogram of the difference between the onset time of the Gaussian function of best-fit SEW of each record and the Gaussian function of the average (unstretched) *S* wave of each event (the first computed SEW, as in Figure 5). The stretched SEW Gaussian minus the unstretched generic empirical wavelet Gaussian is shown. Each color represents histogram from a different phase. SEW = stretched empirical wavelet.

southern hemisphere, but the southern hemisphere, when all the phases are combined, is sampled everywhere. For the upper mantle, the greatest sampling density generally occurs close to earthquake locations. However, SS, SSS, and ScSScS provide additional sampling at their surface reflection locations (e.g., like in the central part of both the Pacific and Atlantic Oceans). Regarding the deepest mantle, there has been abundant attention to large low shear velocity provinces (e.g., Cottaar & Lekic, 2016; Davies, Pozzo, et al., 2015; Davies, Goes, et al., 2015; Garnero & McNamara, 2008; Garnero et al., 2016; Lekic et al., 2012). We anticipate that these data can help resolution in tomographic studies aiming to sharpen imaging of large low shear velocity province structure.

4.6. Stretched Versus Unstretched EW Travel Time Measurements

The onset time measurements reported in this paper involve stretching each event's SEW to best fit every seismic phase of interest for that event. Here we explore how different these measurements would be if there were no stretching of the EW to fit each record. As described in section 3.2 (step 5), a Gaussian function is fit to the stretched SEW for onset time determination of each observation. We also retain the Gaussian function that best fits the SEW that has not been stretched to fit each record (i.e., the representative EW of the *S* wave for each event). We use these two Gaussians to estimate what the onset time difference would be for every measurement in our data set, if we did not stretch the EW to fit each record. The stretched minus unstretched wavelet results are plotted in Figure 15. A negative (or positive) number in this plot corresponds to the observation being broader (or more narrow) than the unstretched EW. The first-order result is that the observed waveform width variability results in significant onset time variability. It is also apparent that longer path lengths (e.g., ScS2 and S3) are broadened significantly beyond the unstretched average wavelet of *S* waves; this is expected from attenuation. However, the spread in the distribution for each phase indicates that using a single pulse for timing determination (e.g., from an EW or synthetic seismograms) will have timing biases due to the variable pulse widths in the observations. We note that there is skew in the distribution (e.g., the direct *S* wave): slightly more *S* waves have later onset times with the SEW compared to an unstretched wavelet. This is due to more *S* waves being slightly narrower than the mean *S* wave width, which is caused by exceptionally broadened *S* waves biasing the mean toward a broader average. This is also indicated in the skewness of the Gaussian factor in Figure 12d for *S* waves. Thus, the zero in Figure 15 is relative to a mean which is biased by the degree to which events are especially broadened pulse widths.

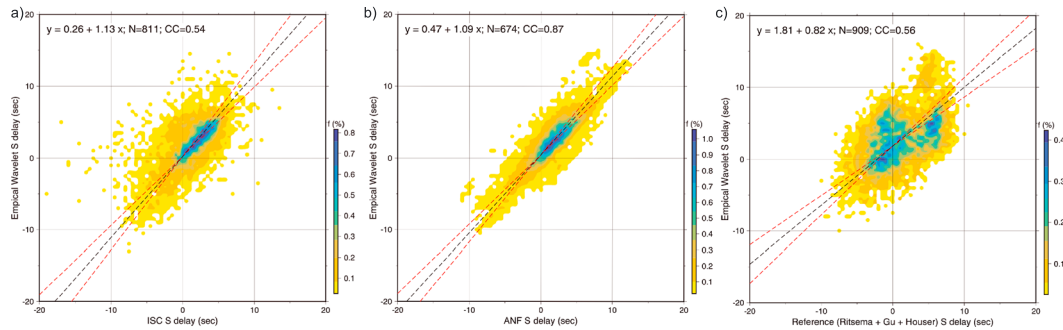


Figure 16. Measured travel time anomalies from our empirical wavelet method are compared to measurements from (a) the ISC bulletin, (b) the ANF catalog, and (c) times reported in three tomographic studies. Summary ray times constructed for small event, and station bins are compared in the figure (thus, every plotted point represents one summary ray comparison). The equation for the best-fitting line is given (black dashed line), along with uncertainty bounds (red dashed lines) for the best fitting line. Also shown is the number of plotted summary ray comparisons (N) and the correlation coefficient (CC) for each best fitting line. Symbols are colored according to the frequency for every 0.5 by 0.5 s time cell on the plot. See text for additional details. ISC = International Seismology Centre; ANF = Array Network Facility.

4.7. Comparison With Previous Data Sets

Various research groups and seismic network operators have implemented largely independent approaches and algorithms to measure travel times. In order to better understand how our new measurements compare with existing data sets, we present relative frequency scatter plots in Figure 16, along with a best-fit linear regression between the data sets. For these plots, the travel time anomalies are relative to predictions based on PREM. The data sets contain different earthquakes and stations, and therefore, we use a summary ray method to find ray paths which are consistent between the data sets. The summary rays average events within 2° latitude by 2° longitude by 50-km depth bins, and station locations are held constant to within 0.01° by 0.01° . For the relative frequency scatter plots, we calculate the relative occurrence of travel time anomalies between the two data sets in 0.5×0.5 s bins. Bins with a frequency of less than 0.02% are removed to reduce the effect of outliers on the linear regression and weights for each point for the regression is taken as $1/\text{frequency}$.

The International Seismological Centre (ISC) compiles and publishes global seismic data. One of their primary products is manually determined travel times distributed through the ISC Bulletin. From this database, we extracted $\sim 635,000$ direct S arrival travel times between 2000 and 2015 (<http://www.isc.ac.uk/iscbulletin/search/arrivals>). These times were then reference to PREM using the TauP toolkit (Crotwell et al., 1999) to compute residuals to compare to our measured residuals. The relationship between S times from our EW method and the ISC times is close to linear (Figure 16a), but there is significant scatter in the ISC data set indicated by the low frequency points at the extremes of the x axis. However, the linear regression line has a low offset (0.27) and a slope of 1.13. The correlation coefficient is fairly low (0.51), but the highest probability points (indicated in green to blue) are well aligned with the 1:1 line. This indicates most of our measurements are well aligned with the ISC data set, but we have fewer large amplitude outliers.

The Array Network Facility (ANF), an Earthscope-USArray funded project largely responsible for the operation of the USArray network, provides manually determined arrival times for the USArray (Astiz et al., 2014). Of the $\sim 2,000,000$ total measurements they have published, $\sim 200,000$ are direct S arrivals. This data set has recently been used for tomography in the United States (Golos et al., 2018), and their results are largely consistent with earlier velocity models for the region. A qualitative comparison of our S times with the ANF times (Figure 16b) shows a clear linear relationship with some scatter. The regression line, using 674 bins, has a slope of 1.09 and an offset of 0.47 s with a correlation coefficient of 0.87. These values and the scatter plot suggest the data sets are highly consistent.

We also compare our S times against a compilation of times from three mantle tomography studies that measured times by various methods (Gu et al., 2005; Houser et al., 2008; Ritsema et al., 2011) in Figure 16c. For this comparison, we have applied crustal corrections (Laske et al., 2013) so that all times are equally adjusted. The apparent scatter for this comparison is greater than both that of the ANF and the ISC. Also, the regression fit is offset by 1.81 s, and the slope is well below 1. The correlation coefficient of 0.56 and

broad scatter of the data points indicate less agreement in our times with some presented in these past studies. One possible source of the misfit is that determination of travel times through correlation approaches (e.g., between synthetic seismograms and observations) do not consider variable waveform pulse widths in the data which result in systematic biases in reported times. We note that with or without crustal corrections, the nature of the scatter in the comparison in Figure 16c does not change.

5. Discussion

This SEW approach presented in this paper was devised to objectively extract arrival time information from data while retaining information about wave-shape broadness (from the stretching, t^* , and Gaussian factor information), complexity (from the misfit and cross-correlation measurements), and signal strength (from SNR measurements). Using the same method on all six phases ensures consistency with this global data set.

All data were visually inspected for every earthquake, but not all data were retained in the data set. Many data were rejected if significant precursors were present that affected the performance of the algorithm to correctly identify the onset time of the waveform. The most common example was for SS waves—a significant opposite polarity precursor was commonly present (even when Hilbert-transformed back into the same phase as the direct S wave). While such data may have good SNR, they were omitted from our measurements due to uncertainties in identifying the onset of the phase.

Our initial processing step involved implementation of a band-pass filter between 16 and 100 s. A shorter period (higher frequency) for the 16-s upper corner in the filter would yield additional information in waveform broadening as well as the potential for sharper waveform onsets. However, for later arriving phases (as well as all phases for shallow ridge events), noise energy around 10-s period was commonly present which obscured clear onsets for many data. The 16-s level for the upper corner of the filter netted significantly more data than broader band filters yet still retained enough short period information for broadening to be detected and measured. While longer-period upper filter corners would likely yield even more measurements, it comes at the cost of losing some shorter period variability in onset times that relates to heterogeneity at smaller scales. As a travel time product-oriented paper, this paper is similar to past papers, for example, like Bolton and Masters (2001) who analyzed ~41,000 S waves, or Woodward and Masters (1991), who measured ~6,000 SS waves (referenced to S). The main difference is our larger data set, shorter periods used, and adaptive waveshape fitting.

A powerful aspect of this data set is the waveform broadening information (e.g., the Gaussian factor). While the computed SEW is a weighted average shape and pulse width, pulse width anomalies relative to the average can be explored in, for example, multipathing or attenuation studies (as well as source studies). Our measured travel times are appropriate for ray theoretical approaches and thus can be used in travel time tomography and forward modeling analyses. However, many approaches are based on the actual seismic waveforms (instead of onset times). There are different ways this data set can be utilized for such studies, including (a) the timing and period information can be used to accurately retrieve the phase of interest from original waveforms, and our data quality information can be utilized to prioritize a data collection scheme and (b) the Gaussian factor information can be used to construct Gaussian functions which approximate every measured waveform—this can even be used in approaches that rely on synthetic seismograms for correlation with waveforms. These possibilities will depend on the focus of any study to be pursued; we present these possibilities to emphasize the flexibility of the data set for mapping mantle velocity and/or attenuation heterogeneity. Future analyses might consider fitting multiple Gaussian functions to complex records to better articulate waveform complexities (e.g., Conder, 2015).

We note that event locations used in this study were taken directly from the ISC and that source relocation has not been done nor has the quality of source locations been assessed. Work using these data for structure determination (e.g., tomography) should, of course, consider event relocation, as well as elevation and crustal corrections. Here we focus on an objective measure of raw travel times relative to a reference model, without correcting for ellipticity. While we emphasize the utility of the EW construction method for the purpose of travel times and whole earth structure studies, it can also be useful in documenting source and site effects, since the provided information can be parsed in terms of source geometry (e.g., azimuth, depth, and take-off angle).

Our method can also be used with other phases, for example, P waves such as P , PcP , $Pdiff$, PKP , etc., and SV waves such as SKS , $SKKS$, etc., as well as depth phases (sS , sSS , etc.) and converted waves (e.g., SP and ScP). Here we chose to develop the method solely with SH waves. Our future plans include application to these other wave types, including higher multiple bounce waves.

6. Conclusions

We developed an EW construction algorithm that adapts an average S wave shape to the six phases S , SS , SSS , $Sdiff$, ScS , and $ScSScS$ for a collection of 360 global earthquakes. From over 1.4 million viewed seismograms, over 251,000 travel times were made with important waveform and waveshape information retained. Our event selection involved strategies to bolster southern hemisphere coverage, especially in the deep mantle. While coverage still remains denser in the northern hemisphere, the southern hemisphere is fairly well sampled in the deepest several 100 km of the mantle. This was mostly accomplished by adding $Sdiff$ but also $ScS2$ and long distance D'' traversing S waves. We have demonstrated that adapting the EW to each record can give onset time measurements that differ by up to several seconds from correlative schemes that use a fixed width reference pulse. This can explain some of the differences between our measurements and past studies. All of these measurements and data attributes are publicly available.

Acknowledgments

This research was financially supported by funds from National Science Foundation (NSF) EAR-1648817. We thank several seismic data centers that provided seismic data for this study, including Incorporated Research Institutions for Seismology, Data Management Center (IRIS DMC), Observatories & Research Facilities for European Seismology (ORFEUS), Northern California Earthquake Data Center (NECDC), F-net Broadband Seismograph Network (F-net), and Canadian National Seismic Network (CNSN). We also thank EarthScope program for the freely available USArray data, which provided large numbers of high-quality seismic data. Moreover, we thank the principle investigators, individuals, and organizations that deployed the seismic networks used in this study. A total number of 308 network codes was used in this study, which correspond to nearly 1,600 unique network deployments from various organizations and groups. We have compiled a list of detailed information of each individual network used in this study, including the network name, network operator, network country, network website if available, network deployment country, and digital object identifier if available. Please refer to Supporting Information S1 for details. Our final data set is available online (<https://zenodo.org/record/1241248>; doi:10.5281/zenodo.1299902). We thank Christine Houser and an anonymous reviewer for exceptionally thoughtful reviews, which helped to improve the manuscript.

References

- Astiz, L., Eakins, J. A., Martynov, V. G., Cox, T. A., Tytell, J., Reyes, J. C., et al. (2014). The Array Network Facility seismic bulletin: Products and an unbiased view of United States seismicity. *Seismological Research Letters*, *85*(3), 576–593. <https://doi.org/10.1785/0220130141>
- Bolton, H., & Masters, G. (2001). Travel times of P and S from the global digital seismic networks: Implications for the relative variation of P and S velocity in the mantle. *Journal of Geophysical Research*, *106*(B7), 13,527–13,540. <https://doi.org/10.1029/2000JB900378>
- Butler, R. (1979). Shear-wave travel times from SS . *Bulletin of the Seismological Society of America*, *22*(2), 231–237. <https://doi.org/10.1121/1.1906594>
- Choy, G. L., & Richards, P. G. (1975). Pulse distortion and Hilbert transformation in multiply reflected and refracted body waves. *Bulletin of the Seismological Society of America*, *22*(2), 231–237. <https://doi.org/10.1121/1.1906594>
- Conder, J. A. (2015). Fitting multiple bell curves stably and accurately to a time series as applied to Hubbert cycles or other phenomena. *Mathematical Geosciences*, *47*(6), 663–678. <https://doi.org/10.1007/s11004-014-9557-7>
- Cottaar, S., & Lekic, V. (2016). Morphology of seismically slow lower-mantle structures. *Geophysical Journal International*, *207*(2), 1122–1136. <https://doi.org/10.1093/gji/ggw324>
- Crotwell, H. P., Owens, T. J., & Ritsema, J. (1999). The TauP Toolkit: Flexible seismic travel-time and ray-path utilities. *Seismological Research Letters*, *70*(2), 154–160. <https://doi.org/10.1785/gssrl.70.2.154>
- Davies, C., Pozzo, M., Gubbins, D., & Alfè, D. (2015). Constraints from material properties on the dynamics and evolution of Earth's core. *Nature Geoscience*, *8*(9), 678–685. <https://doi.org/10.1038/ngeo2492>
- Davies, D. R., Goes, S., & Lau, H. C. P. (2015). Thermally dominated deep mantle LLSVPs: A review. In *The Earth's heterogeneous mantle* (pp. 441–477). Cham: Springer International Publishing.
- Durand, S., Debayle, E., Ricard, Y., Zanolli, C., & Lambotte, S. (2017). Confirmation of a change in the global shear velocity pattern at around 1000 km depth. *Geophysical Journal International*, *211*(3), 1628–1639.
- Dziewonski, A. M., & Anderson, D. L. (1981). Preliminary reference Earth model. *Physics of the Earth and Planetary Interiors*, *25*(4), 297–356. [https://doi.org/10.1016/0031-9201\(81\)90046-7](https://doi.org/10.1016/0031-9201(81)90046-7)
- Dziewonski, A. M., Chou, T. A., & Woodhouse, J. H. (1981). Determination of earthquake source parameters from waveform data for studies of global and regional seismicity. *Journal of Geophysical Research*, *86*(B4), 2825–2852. <https://doi.org/10.1029/JB086iB04p02825>
- Ekström, G., Nettles, M., & Dziewonski, A. M. (2012). The global CMT project 2004–2010: Centroid-moment tensors for 13,017 earthquakes. *Physics of the Earth and Planetary Interiors*, *200–201*, 1–9. <https://doi.org/10.1016/j.pepi.2012.04.002>
- Futterman, W. I. (1962). Dispersive body waves. *Journal of Geophysical Research*, *67*(13), 5279–5291. <https://doi.org/10.1029/JZ067i013p05279>
- Garnero, E. J., & McNamara, A. K. (2008). Structure and dynamics of Earth's lower mantle. *Science*, *320*(5876), 626–628. <https://doi.org/10.1126/science.1148028>
- Garnero, E. J., McNamara, A. K., & Shim, S.-H. (2016). Continent-sized anomalous zones with low seismic velocity at the base of Earth's mantle. *Nature Geoscience*, *9*(7), 481–489. <https://doi.org/10.1038/ngeo2733>
- Golos, M., Fang, H., Yao, H., Zhang, H., Burdick, S., Vernon, F., et al. (2018). Shear wave tomography beneath the United States using a joint inversion of surface and body waves. *Journal of Geophysical Research: Solid Earth*, *123*, 5169–5189. <https://doi.org/10.1029/2017JB014894>
- Grand, S. P. (2002). Mantle shear-wave tomography and the fate of subducted slabs. *Philosophical Transactions of the Royal Society of London. Series A: Mathematical, Physical and Engineering Sciences*, *360*(1800), 2475–2491.
- Gu, Y. H., Lerner-Lam, A. L., Dziewonski, A. M., & Ekström, G. (2005). Deep structure and seismic anisotropy beneath the East Pacific Rise. *Earth and Planetary Science Letters*, *232*(3–4), 259–272. <https://doi.org/10.1016/j.epsl.2005.01.019>
- Houser, C., Masters, G., Shearer, P., & Laske, G. (2008). Shear and compressional velocity models of the mantle from cluster analysis of long-period waveforms. *Geophysical Journal International*, *174*(1), 195–212. <https://doi.org/10.1111/j.1365-246X.2008.03763.x>
- Inoue, H., Fukao, Y., Tanabe, K., & Ogata, Y. (1990). Whole mantle P -wave travel time tomography. *Physics of the Earth and Planetary Interiors*, *59*(4), 294–328. [https://doi.org/10.1016/0031-9201\(90\)90236-Q](https://doi.org/10.1016/0031-9201(90)90236-Q)
- Kustowski, B., Ekström, G., & Dziewonski, A. M. (2008). Anisotropic shear-wave velocity structure of the Earth's mantle: A global model. *Journal of Geophysical Research*, *113*, B06306. <https://doi.org/10.1029/2007JB005169>

- Laske, G., Masters, G., Ma, Z., & Pasyanos, M. (2013). Update on CRUST1.0—A 1-degree global model of Earth's crust. *Geophys. Res. Abstr.*, 15, EGU2013-2658.
- Lekic, V., Cottaar, S., Dziewonski, A., & Romanowicz, B. (2012). Cluster analysis of global lower mantle tomography: A new class of structure and implications for chemical heterogeneity. *Earth and Planetary Science Letters*, 357-358, 68–77. <https://doi.org/10.1016/j.epsl.2012.09.014>
- Lou, X., & van der Lee, S. (2014). Observed and predicted North American teleseismic delay times. *Earth and Planetary Science Letters*, 402, 6–15. <https://doi.org/10.1016/j.epsl.2013.11.056>
- Lou, X., van der Lee, S., & Lloyd, S. (2013). AIMBAT: A python/matplotlib tool for measuring teleseismic arrival times. *Seismological Research Letters*, 84(1), 85–93. <https://doi.org/10.1785/0220120033>
- Ni, S., & Helmberger, D. V. (2003). Ridge-like lower mantle structure beneath South Africa. *Journal of Geophysical Research*, 108(B2), 2094. <https://doi.org/10.1029/2001JB001545>
- Pavlis, G. L., & Vernon, F. L. (2010). Array processing of teleseismic body waves with the USArray. *Computers and Geosciences*, 36(7), 910–920. <https://doi.org/10.1016/j.cageo.2009.10.008>
- Ritsema, J., Deuss, A., Van Heijst, H. J., & Woodhouse, J. H. (2011). S40RTS: A degree-40shear-velocity model for the mantle from new Rayleigh wave dispersion, teleseismic traveltimes and normal-mode splitting function measurements. *Geophysical Journal International*, 184(3), 1223–1236. <https://doi.org/10.1111/j.1365-246X.2010.04884.x>
- Ritsema, J., & van Heijst, H. J. (2002). Constraints on the correlation of P- and S-wave velocity heterogeneity in the mantle from P, PP, PPP and PKPab traveltimes. *Geophysical Journal International*, 149(2), 482–489. <https://doi.org/10.1046/j.1365-246X.2002.01631.x>
- Rost, S. (2002). Array seismology: Methods and applications. *Reviews of Geophysics*, 40(3), 1008. <https://doi.org/10.1029/2000RG000100>
- Schaff, D. P., & Waldhauser, F. (2005). Waveform cross-correlation-based differential travel-time measurements at the northern California seismic network. *Bulletin of the Seismological Society of America*, 95(6), 2446–2461. <https://doi.org/10.1785/0120040221>
- Simmons, N. A., Forte, A. M., Boschi, L., & Grand, S. P. (2010). GyPSuM: A joint tomographic model of mantle density and seismic wave speeds. *Journal of Geophysical Research*, 115, B12310. <https://doi.org/10.1029/2010JB007631>
- To, A., Romanowicz, B., Capdeville, Y., & Takeuchi, N. (2005). 3D effects of sharp boundaries at the borders of the African and Pacific Superplumes: Observation and modeling. *Earth and Planetary Science Letters*, 233(1-2), 137–153. <https://doi.org/10.1016/j.epsl.2005.01.037>
- van der Hilst, R. D., Widiyantoro, S., & Engdahl, E. R. (1997). Evidence for deep mantle circulation from global tomography. *Nature*, 386(6625), 578–584. <https://doi.org/10.1038/386578a0>
- Vandecar, J. C., & Crosson, R. S. (1990). Determination of teleseismic relative phase arrival times using multi-channelcross-correlation and least squares. *Bulletin of the Seismological Society of America*, 91(B14), 13,873–13,169. <https://doi.org/10.1029/JB091iB14p13873>
- Woodhouse, J. H., & Dziewonski, A. M. (1984). Mapping the upper mantle: Three-dimensional modeling of earth structure by inversion of seismic waveforms. *Journal of Geophysical Research*, 89(B7), 5953–5986.
- Woodward, R. L., & Masters, G. (1991). Global upper mantle structure from long-period differential travel times. *Journal of Geophysical Research*, 96(B4), 6351–6377. <https://doi.org/10.1029/90JB01445>